



## Research Article

**Kalman filter based on a fractional discrete-time stochastic augmented CoVid-19 model**

Mohammad Ghani \*, Dwi Rantini, Maryamah

Data Science Technology, Faculty of Advanced Technology and Multidiscipline, Universitas Airlangga, Surabaya 60115, Indonesia

**ARTICLE INFO***Article history:*

Received 30 March 2024

Received in revised form 20 April 2024

Accepted 24 April 2024

*AMS (2020) Subject Classification:*

35A01

35B40

**ABSTRACT**

In this paper, we study the dynamics of the CoVid-19 outbreak in Semarang, Indonesia, using a fractional CoVid-19 model. We first determine the effects of the isolation rate  $\epsilon$  and infection rate  $\beta$  on the reproduction number  $\mathcal{R}_0$  and infected number  $V$ . We find that  $\mathcal{R}_0$  is directly proportional to  $\beta$  and inversely proportional to  $\epsilon$ . For  $V$ , the effect of physical distancing is not as significant as changing  $\epsilon$ . As  $\epsilon$  increases,  $V$  decreases, the number of susceptible individuals increases, the number of quarantined individuals decreases sharply, and the number of recovered individuals decreases. Moreover, the effect of vaccination is also considered. The combination of physical distancing, isolation, and vaccination has a significant impact on reducing the number of infected individuals. Analysis of dynamical systems allows us to understand the characteristics of our model, such as its boundedness and non-negativity, the existence of equilibrium points, the existence and uniqueness of solutions, and the local and global stability. To validate our fractional CoVid-19 model, we introduce the fractional extended Kalman filter (FracEKF) as a prediction method and compare the results against reported CoVid-19 data. FracEKF is a modified version of the basic extended Kalman filter with a time-fractional memory effect. The prediction results illustrate the accuracy of this model in terms of the root mean square error (RMSE), normalized root mean square error (NRMSE), and mean absolute percentage error (MAPE) for each fractional-order. Varying  $\epsilon$  reproduces the trends observed in the reported data for the number of infected individuals, i.e., when  $\epsilon$  increases, the infected number decreases. Moreover, a higher fractional-order results in higher model accuracy. Furthermore, higher values of the process noise  $Q_f$  give smaller errors, whereas higher values of the observation noise  $R_f$  produce higher errors.  $Q_f$  and the fractional-order  $\alpha$  are inversely proportional to RMSE, NRMSE, and MAPE, whereas  $R_f$  is directly proportional to RMSE, NRMSE, and MAPE.

**1. Introduction**

In 2019, the rapid spread of a coronavirus led to the global CoVid-19 outbreak. The symptoms of coronaviruses are fever and shortness of breath. In Indonesia, the CoVid-19 outbreak was first recognized on March 2, 2020.<sup>24</sup> In mid-April of 2023, the Ministry of Health reported the newest Arcturus variant, which had a meaningful impact in Indonesia. This variant was formed by the recombination of two or more homologous sublineages.<sup>39</sup>

Many mathematical models have been employed to provide predictions of the transmission dynamics of CoVid-19. The simplest susceptible-infected (SI) model, derived from the Bernoulli-Verhulst model, can identify various parameters.<sup>20</sup> More complex SIR models consider the recovery aspect, providing predictions of the effects of medical treatment.<sup>3</sup> The SIR model can be used to

reduce the number of outbreak transmissions according to room availability.<sup>6</sup> Cleanliness and physical distancing can help to decrease the transmission of Covid-19,<sup>8</sup> and other studies have examined the effects of local restrictions, short-term comparisons with the Verhulst and Gompertz models, and the influence of the health system on this SIR model.<sup>17,25,5</sup> SIR models can consider the interaction level and intensity of recovery<sup>36</sup> as well as nonstandard finite difference methods.<sup>60</sup>

A parameter-varying modification of the SIRD (Susceptible-Infected-Recovered-Deceased) model was studied in<sup>14</sup> to capture possible structural changes of the epidemic characteristics, and reliable predictions of the short-term infection evolution of CoVid-19 were addressed in.<sup>41</sup> Long-term predictions of the SIRD model for cases in Indonesia have been employed to predict the CoVid-19 outbreak.<sup>42</sup> According to the results, infection is more likely in younger individuals than in older individuals.<sup>16</sup> Another study developed an SEIR (Susceptible-Exposed-Infected-Recovered) model of the CoVid-19 outbreak, including the impact of control

\* Corresponding author.

E-mail address: [mohammad.ghani2013@gmail.com](mailto:mohammad.ghani2013@gmail.com) (M. Ghani).

on exposed sub-individuals in a hybrid model by considering vaccination and isolation.<sup>32,7</sup> The adaptive *SIRV* (Susceptible-Infected-Recovered-Vaccinated) model used the inverse problem approach to estimate the parameters, where the vaccine efficacy reflects the impacts of disease transmission and prevents transmission at the same rate.<sup>40</sup> The hybrid *SVEIR* model employed two vaccination doses and delay effects, where the time delay indicates the time required post-vaccination to provide immunity against SARS-CoV-2.<sup>53</sup> The vaccination campaign was also applied to an *SVIR* model by estimating the parameters using ordinary least-squares<sup>49</sup> and to an *SIQRD* model in which targeted vaccination increased the CoVid-19 vaccine benefits amidst its lack of availability.<sup>26</sup> Moreover, an *SIQR* model<sup>45</sup> has been developed in which the effectiveness of different measures in controlling the outbreak can be investigated. It has been demonstrated that identifying infected patients by polymerase chain reaction testing and isolating them in quarantine is more effective than lockdown measures aimed at restricting physical connections in the general community. Moreover, when employing the hybrid *SIQR* model, environmental noise becomes an important component of the ecosystem.<sup>15</sup> Therefore, it is vital to determine how environmental noise influences epidemic models. Adnan et al.<sup>1</sup> employed the Atangana–Baleanu–Caputo operator for their *SIQR* model of CoVid-19, which promotes quarantine as a means of decreasing transmission and employs the nonstandard finite difference method to approximate the numerical results.<sup>2</sup> Fractional epidemic models have been used to obtain analytical solutions to tumor models with polyclonality and cell mutation,<sup>47</sup> for HPV and co-infection models,<sup>44</sup> for CoVid-19 and viral hepatitis B modeling,<sup>46</sup> for HPV and syphilis transmission using non-singular kernels<sup>43</sup>, and for CoVid-19 incorporating environmental transmission based on Nigerian data.<sup>10</sup> Other studies using fractional-order models include,<sup>4,9,11,12,22,27,51,61,56,57</sup> where the fractional-order captures the current state, memory effects, and long-term interactions in determining the growth rate of the system.

Existing CoVid-19 modeling studies have mostly used deterministic models to identify the model profile through differential equations, but this approach cannot be used to produce stochastic CoVid-19 models.<sup>58,33</sup> Thus, a stochastic model should be developed. In addition to epidemiological models, a real-time algorithm for estimating the transmission state is required for the dynamic modeling of the CoVid-19 pandemic. The recursive least-squares (RLS) method is widely used for estimating model parameters.<sup>52,37</sup> RLS can estimate the optimal states by determining the minimum linear LS objective function with respect to the system observations. The Kalman filter (KF) represents an improvement over RLS, using the states of RLS to obtain predictive results. Moreover, Monte Carlo-based analysis can be employed to fit fractional CoVid-19 models to actual data.<sup>35,55</sup> Monte Carlo sampling has been used to analyze the spreading profile of the coronavirus disease in the United States via time-variant reliability analysis,<sup>54</sup> while the network autoregressive model has been used to predict the CoVid-19 spread by considering the disease interaction in neighboring countries.<sup>34</sup> The extended Kalman filter (EKF) improves the original KF by linearizing the nonlinear dynamical system.

The EKF provides a simple algorithm for solving nonlinear dynamical systems when compared with constrained least-squares (CLS) and Markov chain Monte Carlo (MCMC).<sup>23,63</sup> Hassan et al. introduced an EKF for an *SEIR* model of CoVid-19 in which the exposed individuals and incubation period were not considered.<sup>29</sup> To predict CoVid-19 transmission, an EKF was applied to the Lotka–Volterra model<sup>13</sup> under a capacity limitation to establish the complex natural transmission dynamics of CoVid-19. Moreover, research on CoVid-19 hybrid model estimation has been conducted using a novel EKF for the maximum likelihood.<sup>58</sup> However,

this EKF of maximum likelihood arises from a deterministic model, so the stochastic CoVid-19 dynamics cannot be characterized, and neglects re-infection and physical distancing.

The model proposed in this paper is based on previous studies<sup>18,19</sup> in which the growth rates provide the current state, without considering physical distancing ( $\delta$ ) and the isolation rate ( $\epsilon$ ). This paper considers the Caputo fractional derivative, which is defined as follows.

**Definition 1.** (See<sup>50,48,59</sup>). Let  $\alpha > 0$ . Then, for some function  $f \in C^n$ , the Caputo fractional derivative with order  $\alpha$  is given by

$$D_*^\alpha f(t) = \frac{1}{\Gamma(n-\alpha)} \int_0^t \frac{f^{(n)}(s)}{(t-s)^{1+\alpha-n}} ds, \quad (1)$$

where  $n = \lceil \alpha \rceil$ .

For the particular case of  $0 < \alpha \leq 1$ , Eq. (1) can be written as follows:

$$D_*^\alpha f(t) = \frac{1}{\Gamma(1-\alpha)} \int_0^t \frac{f'(s)}{(t-s)^\alpha} ds. \quad (2)$$

The nonlocal operator of the Caputo fractional derivative (i.e., the initial and current states are considered<sup>30,31</sup>) allows us to modify the dynamical system in<sup>18,19</sup> and consider both physical distancing  $\delta$  and the isolation rate  $\epsilon$ . Therefore, the first derivatives of the dynamical system in<sup>18,19</sup> are replaced by the Caputo fractional derivative to obtain

$$\begin{aligned} D_*^\alpha U &= \Lambda - \beta \delta UV - \psi U, \\ D_*^\alpha V &= \beta \delta UV - (r + \epsilon + \psi + d)V, \\ D_*^\alpha W &= \epsilon V - (\kappa + d + \psi)W, \\ D_*^\alpha Z &= rV + \kappa W - \psi Z, \end{aligned} \quad (3)$$

where  $U(0) = U_0, V(0) = V_0, W(0) = W_0, Z(0) = Z_0, 0 < \alpha \leq 1$ . A description of all model parameters is presented in Table 1. The values for physical distancing range from 0 (the highest level of physical distancing) to 1 (the lowest level of physical distancing). As shown in Fig. 1, susceptible individuals  $U$  that come into contact with the disease become infected individuals  $V$  according to the transmission rate  $\beta$ . The number of infected individuals decreases if the physical distancing parameter  $\delta$  increases. The infected individuals  $V$  become either quarantined individuals  $W$  or recovered individuals  $Z$ . The infected individuals become quarantined individuals according to the isolation rate  $\epsilon$  if the symptoms worsen and they require treatment. Moreover, the infected individuals become recovered individuals according to the recovery rate  $r$  if the symptoms decrease as the immune system fights the infection. The quarantined individuals  $W$  become recovered individuals  $Z$  if the symptoms decrease as a result of the immune system and the treatment received during the quarantine period. The mortality rate  $d$  from CoVid-19 is applied during the infection and quarantine period, and there is also the natural mortality  $\psi$  caused by factors other

**Table 1**

Model parameter and sensitivity index (SI), where all parameters are assumed and the values of SI are based on the calculations in Eqs. (5)–(12).

Parameter	Description	Value	SI
$\Lambda$	Birth rate	0.07	1
$\beta$	Infection rate	0.057	1
$\delta$	Physical distancing rate	0.4	1
$\psi$	Natural mortality rate	0.0019	-1
$r$	Recovery rate of infected individuals	0.057	-0.4410
$\epsilon$	Isolation rate	0.03	-0.4410
$d$	Mortality rate of infected and isolated individuals	0.001	-0.1176
$\kappa$	Recovery rate of isolated individuals	0.7	-

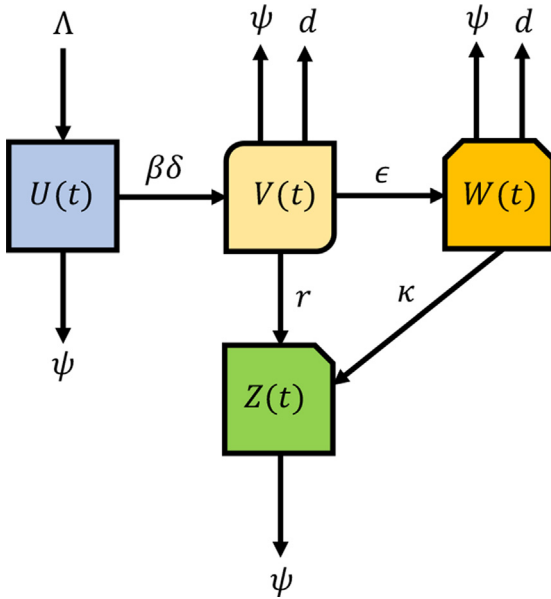


**Fig. 1.** 1st compartment diagram of CoVid-19 model.

than CoVid-19. An EKF is employed to give predictive results based on reported CoVid-19 data. The memory effect and long-rate interactions in the proposed model mean that the EKF must be modified for the fractional-order stochastic CoVid-19 model. Therefore, we introduce a fractional EKF (FracEKF) to overcome the memory effect of our fractional-order CoVid-19 model.

## 2. Model analysis

**Lemma 1.** (See<sup>28</sup>). Suppose that the fractional-order  $0 < \alpha \leq 1$  exists and consider the continuous function  $\varphi(t)$  in  $\mathbb{R}_+$ . One can then derive

$$D_*^\alpha \left( \varphi(t) - \varphi^* - \varphi^* \ln \frac{\varphi(t)}{\varphi^*} \right) \leq \left( 1 - \frac{\varphi^*}{\varphi(t)} \right) D_*^\alpha \varphi(t), \quad (4)$$

where  $\varphi^* \in \mathbb{R}_+$  and  $t > 0$ .

### 2.1. Property of boundedness and non-negativity

**Theorem 2.1.** All variables  $(U, V, W, Z)(t) \geq 0$  in a region  $\Pi = \{N(t) \in \mathbb{R}^4 : N(t) \leq \frac{\Lambda}{\psi}\}$  are bounded for all  $t > 0$ .

#### Proof.

Let the total number of individuals in our CoVid-19 model be defined as  $N(t) = (U + V + W + Z)(t)$ , which satisfies

$$D_*^\alpha N(t) \leq \Lambda - \psi N(t).$$

Employing the standard comparison technique (Theorem 1,<sup>28</sup>) yields

$$\begin{aligned} N(t) &\leq N(0) \mathcal{M}_\alpha(-\psi t^\alpha) \\ &+ \frac{\Lambda}{\psi} (1 - \mathcal{M}_\alpha(-\psi t^\alpha)) \quad (\mathcal{M}_\alpha \text{ is Mittage-Leffler function}). \end{aligned}$$

As  $t \rightarrow +\infty$ , we have that  $\mathcal{M}_\alpha(-\psi t^\alpha) \approx 0$ . Consequently, we find that

$$\lim_{t \rightarrow +\infty} \sup N(t) \leq \frac{\Lambda}{\psi}.$$

**Theorem 2.2.** Let  $(U, V, W, Z)(0) \geq 0$  be the initial data of dynamical system (3). Then, for all  $t > 0$ , we have that  $(U, V, W, Z)(t) \geq 0$ .

#### Proof.

According to the first equation of (3), we have

$$\begin{aligned} D_*^\alpha U(t) &= \Lambda - \beta\delta UV - \psi U \\ &\geq -(\beta\delta V + \psi)U = -\left(\frac{\Lambda\beta\delta}{\psi} + \psi\right)U. \end{aligned}$$

It follows from the standard comparison technique (Theorem 1,<sup>28</sup>) that

$$U(t) \geq (U(0) - 0) \mathcal{M}_\alpha \left( -\left(\frac{\Lambda\beta\delta}{\psi} + \psi\right) t^\alpha \right) \quad (\mathcal{M}_\alpha \text{ is Mittage-Leffler function}).$$

Because  $\mathcal{M}_\alpha \left( -\left(\frac{\Lambda\beta\delta}{\psi} + \psi\right) t^\alpha \right) \approx 0$  as  $t \rightarrow +\infty$ , it follows that  $U(t) \geq 0$ . Similarly, for the Mittage-Leffler functions  $\mathcal{M}_\alpha(-(r + \epsilon + \psi + d)t^\alpha)$ ,  $\mathcal{M}_\alpha(-(\kappa + d + \psi)t^\alpha)$ , and  $\mathcal{M}_\alpha(-\psi t^\alpha)$ , we have that  $(V, W, Z)(t) \geq 0$  as  $t \rightarrow +\infty$ .

### 2.2. Equilibrium point

**Theorem 2.3.** When  $\mathcal{R}_0 < 1$ , the disease-free equilibrium point  $\mathcal{E}_0^0 = \left(\frac{\Lambda}{\psi}, 0, 0, 0\right)$  is established. When  $\mathcal{R}_0 > 1$ , the endemic equilibrium point  $\mathcal{E}_0^*$  is given by

$$\mathcal{E}_0^* = \left( \frac{r + \epsilon + \psi + d}{\beta\delta}, \frac{\Lambda}{r + \epsilon + \psi + d} - \frac{\psi}{\beta\delta}, \frac{\epsilon}{\kappa + d + \psi} V^*, \frac{rV^*}{\psi} + \frac{\kappa W^*}{\psi} \right)$$

#### Proof.

The proof is obtained by employing the steady state, i.e.,  $D_*^\alpha U(t) = D_*^\alpha V(t) = D_*^\alpha W(t) = D_*^\alpha Z(t) = 0$  for all  $t > 0$  and  $V = W = 0$  in the disease-free state,  $V \neq 0, W \neq 0$  when the disease is endemic.

The next step is to determine the basic reproduction number  $\mathcal{R}_0$ , which is important in epidemiological models. The basic reproduction number consists of two aspects, i.e., the transmission matrix  $\mathcal{F}$  and the transition matrix  $\mathcal{V}$ , which are given as follows:

$$\mathcal{F} = \begin{pmatrix} \beta\delta U & 0 \\ 0 & 0 \end{pmatrix}, \quad \mathcal{V} = \begin{pmatrix} (r + \epsilon + \psi + d) & 0 \\ -\epsilon & \kappa + d + \psi \end{pmatrix}.$$

Based on the existence of equilibrium points in the disease-free state and the calculation of the next generation matrix  $\mathcal{F}\mathcal{V}^{-1}$ ,<sup>21</sup> we consider the following basic reproduction number for our dynamical system:

$$\mathcal{R}_0 = \frac{\Lambda\beta\delta}{\psi(r + \epsilon + \psi + d)}. \quad (5)$$

### 2.3. Property of existence and uniqueness

**Theorem 2.4.** There exists  $(\kappa_1, \kappa_2)(t) \in L^1(0, T) \times L^w(0, T)$  and  $t \in [0, T]$  where  $w > 1$  for a positive maximum time span  $T$ . Then, the function  $\mathcal{K} : [0, T] \times \mathbb{R} \rightarrow \mathbb{R}$  satisfies the following conditions:

$$\sup_{u \in \mathbb{R}} |\mathcal{K}(t, u)| \leq \kappa_1(t), \quad \sup_{u, v \in \mathbb{R}, u \neq v} \frac{|\mathcal{K}(t, u) - \mathcal{K}(t, v)|}{|u - v|} \leq \kappa_2(t).$$

Moreover, for any  $p_0 \in \mathbb{R}$ , we can express Eq. (3) in the following general form:

$$\begin{aligned} D_*^\alpha P(t) &= \mathcal{K}(t, P(t)), \\ P(0) &= p_0, \end{aligned} \quad (6)$$

for almost every  $t \in [0, T]$  and uniquely continuous  $P : [0, T] \rightarrow \mathbb{R}$ .

### Proof.

Employing the Riemann–Liouville fractional integral, Eq. (6) can be written as

$$P(t) = p_0 + \frac{1}{\Gamma(\alpha)} \int_0^t (t - \xi)^{(\alpha-1)} \mathcal{K}(\xi, P(\xi)) d\xi, \quad t \in [0, T]. \quad (7)$$

According to Picard's iteration, Eq. (7) becomes

$$\begin{aligned} P_{n+1}(t) &= p_0 + \frac{1}{\Gamma(\alpha)} \int_0^t (t - \xi)^{(\alpha-1)} \mathcal{K}(\xi, P_n(\xi)) d\xi, \\ P_0(t) &= p_0. \end{aligned}$$

The continuity of  $P_n : [0, T] \rightarrow \mathbb{R}$  for each  $n$  yields

$$\begin{aligned} \|P_n - p_0\|_{L^\infty(0,T)} &\leq \frac{1}{\Gamma(\alpha)} \left( \int_0^t (t - \xi)^{\frac{\alpha-1}{1-w}} d\xi \right)^{1-w} \left( \int_0^t t_*^{\frac{1}{w}} d\xi \right)^w \sup_{P_{n-1} \in \mathbb{R}} |\mathcal{K}(\xi, P_n(\xi))| d\xi \\ &\leq \frac{t_*^{\frac{1}{w}(1-w)T^{2-1}}}{(x-w)\Gamma(\alpha)} \int_0^t \kappa_1(\xi) d\xi \leq \frac{t_*^{\frac{1}{w}(1-w)T^{2-1}}}{(x-w)\Gamma(\alpha)} \|\kappa_1\|_{L^1(0,T)}. \\ \|P_{n+1} - P_n\|_{L^\infty(0,T)} &\leq \frac{1}{\Gamma(\alpha)} \left( \int_0^t (t - \xi)^{\frac{\alpha-1}{1-w}} d\xi \right)^{1-w} \left( \int_0^t t_*^{\frac{1}{w}} d\xi \right)^w \\ &\quad \sup_{(P_n, P_{n-1}) \in \mathbb{R}, P_n \neq P_{n-1}} |\mathcal{K}(\xi, P_n(\tau)) - \mathcal{K}(\xi, P_{n-1}(\xi))| d\xi \\ &\leq \frac{t_*^{\frac{1}{w}(1-w)T^{2-1}}}{(x-w)\Gamma(\alpha)} \sup_{(P_n, P_{n-1}) \in \mathbb{R}, P_n \neq P_{n-1}} \left| \int_0^t (P_n(\xi) - P_{n-1}(\xi)) d\xi \right| \int_0^t \kappa_2(\xi) d\xi \\ &\leq \frac{t_*^{\frac{1}{w}(1-w)T^{2-1}}}{(x-w)\Gamma(\alpha)} \sup_{(P_n, P_{n-1}) \in \mathbb{R}, P_n \neq P_{n-1}} \left| \int_0^t (P_n(\xi) - P_{n-1}(\xi)) d\xi \right| \int_0^t (\kappa_2(\xi))^{\frac{1}{w}} (t_*)^{1-\frac{1}{w}} d\xi \\ &\leq \frac{t_*^{\frac{1}{w}(1-w)T^{2-1}} \|\kappa_2\|_{L^p} t_*^{\frac{1}{w}}}{(x-w)\Gamma(\alpha)} \sup_{(P_n, P_{n-1}) \in \mathbb{R}, P_n \neq P_{n-1}} \left| \int_0^t (P_n(\xi) - P_{n-1}(\xi)) d\xi \right| \\ &\leq \frac{(1-w)T^{2-1} \|\kappa_2\|_{L^p} t_*}{(x-w)\Gamma(\alpha)} \|P_n - P_{n-1}\|_{L^\infty(0,T)}, \end{aligned} \quad (8)$$

where  $t_* \leq T$ . Using the similarity of the norms of  $\|P_n - P_{n-1}\|$ ,  $\|P_{n-1} - P_{n-2}\|$  until  $\|P_1 - P_0\|$  in  $L^\infty(0, T)$ , we can derive

$$\begin{aligned} \|P_{n+1} - P_n\|_{L^\infty(0,T)} &\leq \frac{(1-w)T^{2-1} \|\kappa_2\|_{L^p} t_*}{(x-w)\Gamma(\alpha)} \|P_n - P_{n-1}\| \leq \dots \leq \left( \frac{(1-w)T^{2-1} \|\kappa_2\|_{L^p} t_*}{(x-w)\Gamma(\alpha)} \right)^n \|\kappa_1\|_{L^1(0,T)}, \end{aligned}$$

which completes the proof of existence. The uniqueness is proved by assuming  $r(t) = (r_1 - r_2)(t)$ . Then, we can write

$$\begin{aligned} \|r\|_{L^\infty(0,T)} &\leq \frac{1}{\Gamma(\alpha)} \left( \int_0^t (t - \xi)^{\frac{\alpha-1}{1-w}} d\xi \right)^{1-w} \left( \int_0^t t_*^{\frac{1}{w}} d\xi \right)^w \sup_{(r_1, r_2) \in \mathbb{R}, r_1 \neq r_2} |r_1(\xi) - r_2(\xi)| d\xi \int_0^t \kappa_2(\xi) d\xi \\ &\leq \frac{t_*^{\frac{1}{w}(1-w)T^{2-1}}}{(x-w)\Gamma(\alpha)} \|r\|_{L^\infty(0,T)} \int_0^t (\kappa_2(\xi))^{\frac{1}{w}} (t_*)^{1-\frac{1}{w}} d\xi \\ &\leq \frac{(1-w)T^{2-1} \|r\|_{L^\infty(0,T)}}{(x-w)\Gamma(\alpha)} \|r\|_{L^\infty(0,T)}. \end{aligned}$$

Because  $w > 1$  and  $0 < \alpha \leq 1$ , the right-hand side must be smaller than the left-hand side for a maximum time span of  $T > 0$ , which provides the contradiction (the state variables are never negative). The solution is then obtained only if  $\|r\|_{L^\infty(0,T)} = 0$  or  $r_1 = r_2$ , indicating the uniqueness of the solution.

### 2.4. Stability

**Theorem 2.5.** When  $\mathcal{R}_0 < 1$ , the solution is locally asymptotically stable at the disease-free equilibrium point  $(\mathcal{E}_\beta^0)$ . When  $\mathcal{R}_0 > 1$ , the solution is locally asymptotically stable at the endemic equilibrium point  $(\mathcal{E}_\beta^*)$ .

### Proof.

The proof is obtained by examining the eigenvalues of the following Jacobian matrix:

$$J(\mathcal{E}_\beta^0) = \begin{pmatrix} -\psi & -\frac{\Lambda\beta\delta}{\psi} & 0 & 0 \\ 0 & \frac{\Lambda\beta\delta}{\psi} - (r + \epsilon + \psi + d) & 0 & 0 \\ 0 & \epsilon & -(\kappa + d + \psi) & 0 \\ 0 & r & \kappa & -\psi \end{pmatrix}.$$

Using the formula  $\det(J(\mathcal{E}_\beta^0) - \lambda I) = 0$  for this Jacobian matrix, we obtain the characteristic equation

$$(-\psi - \lambda)^2(-(\kappa + d + \psi) - \lambda) \left( \frac{\Lambda\beta\delta}{\psi} - (r + \epsilon + \psi + d) - \lambda \right) = 0.$$

Thus, we compute the eigenvalues  $\lambda_1 = \lambda_2 = -\psi < 0$ ,  $\lambda_3 = -(\kappa + d + \psi) < 0$ , and  $\lambda_4 = (r + \epsilon + \psi + d)(\mathcal{R}_0 - 1) < 0$  if  $\mathcal{R}_0 < 1$ .

The next step is to determine the local stability of the endemic equilibrium point, which is obtained based on the Routh–Hurwitz criterion. Similarly, we have the following Jacobian matrix:

$$J(\mathcal{E}_\beta^*) = \begin{pmatrix} -\beta\delta V^* - \psi & -\beta\delta U^* & 0 & 0 \\ \beta\delta V^* & \beta\delta U^* - (r + \epsilon + \psi + d) & 0 & 0 \\ 0 & \epsilon & -(\kappa + d + \psi) & 0 \\ 0 & r & \kappa & -\psi \end{pmatrix}.$$

The formula  $\det(J(\mathcal{E}_\beta^*) - \lambda I) = 0$  is applied for this Jacobian matrix, and we compute the eigenvalues  $\lambda_1 = -\psi < 0$ ,  $\lambda_2 = -(\kappa + d + \psi) < 0$ , and

$$\lambda_3 + \lambda_4 = \text{Tr}(J(\mathcal{E}_\beta^*)) = -\frac{\Lambda\beta\delta}{r+\epsilon+\psi+d} < 0,$$

$$\lambda_3 \cdot \lambda_4 = \text{Det}(J(\mathcal{E}_\beta^*)) = \psi(\mathcal{R}_0 - 1)(r + \epsilon + \psi + d) + \frac{\Lambda\beta\delta}{r+\epsilon+\psi+d} > 0.$$

Moreover, the polynomial  $p(\lambda) = \lambda^2 + c_1\lambda + c_2$  satisfies the Routh–Hurwitz criterion, i.e.,  $c_1 > 0$  and  $c_1 \cdot c_2 > 0$ . This completes the proof.

**Theorem 2.6.** When  $\mathcal{R}_0 < 1$ , the solution is globally asymptotically stable at the disease-free equilibrium point  $(\mathcal{E}_\beta^0)$ . When  $\mathcal{R}_0 > 1$ , the solution is globally asymptotically stable at the endemic equilibrium point  $(\mathcal{E}_\beta^*)$ .

### Proof.

For the disease-free equilibrium point  $(\mathcal{E}_\beta^0)$ , we first provide the Lyapunov function

$$\mathcal{L}_F = \left( U - U^0 - U^0 \ln \frac{U}{U^0} \right) + \frac{(r + \epsilon)V}{r + \epsilon + \psi + d} + \frac{\kappa W}{\kappa + d + \psi} + Z.$$

Employing Lemma 1, we can derive

$$D_*^\alpha \mathcal{L}_F \leq \left( \frac{U - U^0}{U} \right) D_*^\alpha U + \frac{(r + \epsilon)D_*^\alpha V}{r + \epsilon + \psi + d} + \frac{\kappa D_*^\alpha W}{\kappa + d + \psi} + D_*^\alpha Z.$$

According to  $\Lambda = \psi U^0$  and  $\Lambda = \psi Z^0$ , we have that

$$\begin{aligned} D_*^\alpha \mathcal{L}_F &\leq \left( \frac{U - U^0}{U} \right) \left( \psi(U^0 - U) - \beta\delta UV \right) + \frac{(r + \epsilon)(\beta\delta UV - (r + \epsilon + \psi + d)V)}{r + \epsilon + \psi + d} \\ &\quad + \frac{\kappa(\epsilon V - (\kappa + d + \psi)W)}{\kappa + d + \psi} + (rV + \kappa W - \psi Z). \end{aligned}$$

From  $U(t) \leq \frac{\Lambda}{\psi}$  and  $\beta\delta UV = \Lambda - \psi U$ , we find that

$$\begin{aligned} D_*^\alpha \mathcal{L}_F &\leq -\psi \frac{(U - U^0)^2}{U} - (1 - \mathcal{R}_0)(r + \epsilon + \psi + d)V \\ &\quad - (\kappa + d + \psi)W - \frac{(r + d)\Lambda}{\psi}Z. \end{aligned} \quad (9)$$

Moreover, the right-hand side in Eq. (9) is defined as follows:

$$\begin{aligned} \mathcal{B}(t) &= \psi \frac{(U - U^0)^2}{U} + (1 - \mathcal{R}_0)(r + \epsilon + \psi + d)V + (\kappa + d + \psi)W \\ &\quad + \frac{(r + d)\Lambda}{\psi}Z. \end{aligned}$$

Because  $\mathcal{R}_0 < 1$ , the function  $\mathcal{B}(t)$  is positive. Then, Eq. (9) becomes  $D_*^\alpha \mathcal{L}_F(t) \leq -\mathcal{B}(t)$ , implying that  $\mathcal{L}_F(t) + J^\alpha \mathcal{B}(t) \leq \mathcal{L}_F(0) = C$ , where  $J^\alpha$  is the operator of integration with fractional-order  $\alpha$ . Hence,

$$J^\alpha \left( \frac{(U - U^0)^2}{U} \right) \leq C, J^\alpha V \leq C, J^\alpha W \leq C \text{ and } J^\alpha Z \leq C.$$

Using Barbalat's theorem and uniform continuity,<sup>62</sup> we have  $U \rightarrow U^0$  as  $t \rightarrow \infty$ ,  $V \rightarrow 0$  as  $t \rightarrow \infty$ ,  $W \rightarrow 0$  as  $t \rightarrow \infty$ , and  $Z \rightarrow 0$  as  $t \rightarrow \infty$ . Therefore,  $(U, V, W, Z) \rightarrow (\frac{\Lambda}{\psi}, 0, 0, 0)$  as  $t \rightarrow \infty$  for initial data in the bounded region  $\Pi$ .

Similarly, to prove the global stability of endemic equilibrium point  $(\mathcal{E}_\mathcal{P}^*)$ , we provide the following Lyapunov function:

$$\mathcal{L}_F = \mathcal{L}_{F_1}(U) + \mathcal{L}_{F_2}(V) + \mathcal{L}_{F_3}(W) + \mathcal{L}_{F_4}(Z),$$

where

$$\begin{aligned} \mathcal{L}_{F_1}(U) &= (U - U^* - U^* \ln \frac{U}{U^*}), \\ \mathcal{L}_{F_2}(V) &= (V - V^* - V^* \ln \frac{V}{V^*}), \\ \mathcal{L}_{F_3}(W) &= (W - W^* - W^* \ln \frac{W}{W^*}), \\ \mathcal{L}_{F_4}(Z) &= (Z - Z^* - Z^* \ln \frac{Z}{Z^*}). \end{aligned}$$

From Lemma 1, we have

$$\begin{aligned} D_*^\alpha \mathcal{L}_F &\leq (1 - \frac{U}{U^*})D_*^\alpha + (1 - \frac{V}{V^*})D_*^\alpha + (1 - \frac{W}{W^*})D_*^\alpha + (1 - \frac{Z}{Z^*})D_*^\alpha \\ &\leq \mathcal{P}_1 + \mathcal{P}_2 + \mathcal{P}_3 + \mathcal{P}_4, \end{aligned}$$

where

$$\begin{aligned} \mathcal{P}_1 &= (1 - \frac{U}{U^*})(\Lambda - \beta\delta UV - \psi U), \\ \mathcal{P}_2 &= (1 - \frac{V}{V^*})(\beta\delta UV - (r + \epsilon + \psi + d)V), \\ \mathcal{P}_3 &= (1 - \frac{W}{W^*})(\epsilon V - (\kappa + d + \psi)W), \\ \mathcal{P}_4 &= (1 - \frac{Z}{Z^*})(rV + \kappa W - \psi Z). \end{aligned} \quad (10)$$

Using  $U = U - U^*$ ,  $V = V - V^*$ ,  $W = W - W^*$ , and  $Z = Z - Z^*$  in Eq. (10), we can derive

$$\begin{aligned} D_*^\alpha \mathcal{L}_F &\leq (1 - \frac{U}{U^*})(\Lambda - \beta\delta(U - U^*)(V - V^*) - \psi(U - U^*)) + \\ &\quad (1 - \frac{V}{V^*})(\beta\delta(U - U^*)(V - V^*) - (r + \epsilon + \psi + d)(V - V^*)) + \\ &\quad (1 - \frac{W}{W^*})(\epsilon(V - V^*) - (\kappa + d + \psi)(W - W^*)) + \\ &\quad (1 - \frac{Z}{Z^*})(r(V - V^*) + \kappa(W - W^*) - \psi(Z - Z^*)). \end{aligned}$$

After simplifying this expression, we find that  $D_*^\alpha \mathcal{L}_F \leq \mathcal{Q}_1 - \mathcal{Q}_2$ , where

$$\begin{aligned} \mathcal{Q}_1 &= \Lambda + \frac{\beta\delta V^*(U - U^*)^2}{U} + \frac{\beta\delta U(V - V^*)^2}{V} + \frac{\epsilon(VW + V^*W^*)}{W} + \\ &\quad \frac{r(VZ + V^*Z^*)}{Z} + \frac{\kappa(WZ + W^*Z^*)}{Z}, \\ \mathcal{Q}_2 &= \frac{\Lambda U^*}{U} + \frac{(\beta\delta V + \psi)(U - U^*)^2}{U} + \frac{(\beta\delta U^* + r + \epsilon + \psi + d)(V - V^*)^2}{V} + \\ &\quad \frac{\epsilon(V^*W + VW^*)}{W} + \frac{(\kappa + d + \psi)(W - W^*)^2}{W} + \frac{r(V^*Z + VZ^*)}{Z} + \\ &\quad \frac{\kappa(W^*Z + WZ^*)}{Z} + \frac{\psi(Z - Z^*)^2}{Z}. \end{aligned}$$

Therefore,  $D_*^\alpha \mathcal{L}_F < 0$  if  $\mathcal{Q}_1 - \mathcal{Q}_2 < 0$  and  $\mathcal{Q}_1 - \mathcal{Q}_2 = 0$  if  $U = U^*$ ,  $V = V^*$ ,  $W = W^*$ ,  $Z = Z^*$ , implying that  $D_*^\alpha \mathcal{L}_F = 0$ . Hence,  $D_*^\alpha \mathcal{L}_F \leq \mathcal{Q}_1 - \mathcal{Q}_2 = -\mathcal{G}(t)$ , where  $\mathcal{G}(t)$  is a positive function. The integration results are then obtained as  $\mathcal{L}_F(t) + J^\alpha \mathcal{G}(t) \leq \mathcal{L}_F(0) = C$ , where  $J^\alpha$  is the operator of integration for the fractional-order  $\alpha$ . Moreover, we can derive

$$\begin{aligned} J^\alpha \left( \frac{(U - U^*)^2}{U} \right) &\leq C, J^\alpha \left( \frac{(V - V^*)^2}{V} \right) \leq C, J^\alpha \left( \frac{(W - W^*)^2}{W} \right) \leq C \\ \text{and } J^\alpha \left( \frac{(Z - Z^*)^2}{Z} \right) &\leq C. \end{aligned}$$

Based on Barbalat's theorem and uniform continuity,<sup>62</sup> we find that  $U \rightarrow U^*$  as  $t \rightarrow \infty$ ,  $V \rightarrow V^*$  as  $t \rightarrow \infty$ ,  $W \rightarrow W^*$  as  $t \rightarrow \infty$ , and  $Z \rightarrow Z^*$  as  $t \rightarrow \infty$ . Therefore,  $(U, V, W, Z) \rightarrow (U^*, V^*, W^*, Z^*)$  as  $t \rightarrow \infty$  for initial data in the bounded region  $\Pi$ .

### 3. Proposed method

The purpose of this section is to compare the predictive results given by our model (3) and the reported CoVid-19 data using FracEKF. The whole process is illustrated in Fig. 2. As shown in Fig. 2, FracEKF consists of predicting and updating steps, where  $F(\bar{Y}(\zeta|\zeta))$  is the right-hand side of (3),  $J(\bar{Y}(\zeta|\zeta))$  is the Jacobian matrix (obtained from the derivatives of each state variable), and two fixed values of the process noise  $Q_f$  and the observation noise  $R_f$ . Following a previous study<sup>38</sup> that reported time-fractional numerical results, we modify the EKF by considering the memory effect to give an accurate time-fractional-order of  $1 - \alpha$ . Therefore, the iterative form is

$$\hat{Y}(\zeta + 1) = \hat{Y}(\zeta) - E + \Gamma(1 - \alpha) \times (\Delta t)^\alpha \times F(\hat{Y}(\zeta)) + Q_f(\zeta),$$

where  $E$  is the memory effect, which is defined as

$$E = \sum_{\eta=1}^{\zeta} [(\eta + 1)^{1-\alpha} - \eta^{1-\alpha}] [\hat{Y}(\zeta + 1 - \eta) - \hat{Y}(\zeta - \eta)].$$

Moreover,  $Q_f$  shows the covariance of the process and  $F(\hat{Y}(m))$  shows the right-hand side of dynamical system (3), where  $\hat{Y}$  provides all state variables  $U, V, W, Z$ . Applying the two equations stated above in dynamical system (3), we have

$$\begin{aligned} U^{\zeta+1} &= U^\zeta - E_U + \Gamma(1 - \alpha) \times (\Delta t)^\alpha \times (\Lambda - \beta\delta U^\zeta V^\zeta - \psi U^\zeta) + Q_{f1}^\zeta, \\ V^{\zeta+1} &= V^\zeta - E_V + \Gamma(1 - \alpha) \times (\Delta t)^\alpha \times (\beta\delta U^\zeta V^\zeta - (r + \epsilon + \psi + d)V^\zeta) + Q_{f2}^\zeta, \\ W^{\zeta+1} &= W^\zeta - E_W + \Gamma(1 - \alpha) \times (\Delta t)^\alpha \times (\epsilon V^\zeta - (\kappa + d + \psi)W^\zeta) + Q_{f3}^\zeta, \\ Z^{\zeta+1} &= Z^\zeta - E_Z + \Gamma(1 - \alpha) \times (\Delta t)^\alpha \times (rV^\zeta + \kappa W^\zeta - \psi Z^\zeta) + Q_{f4}^\zeta, \end{aligned}$$

where

$$\begin{aligned} E_U &= \sum_{\eta=1}^{\zeta} [(\eta + 1)^{1-\alpha} - \eta^{1-\alpha}] [U(\zeta + 1 - \eta) - U(\zeta - \eta)], \\ E_V &= \sum_{\eta=1}^{\zeta} [(\eta + 1)^{1-\alpha} - \eta^{1-\alpha}] [V(\zeta + 1 - \eta) - V(\zeta - \eta)], \\ E_W &= \sum_{\eta=1}^{\zeta} [(\eta + 1)^{1-\alpha} - \eta^{1-\alpha}] [W(\zeta + 1 - \eta) - W(\zeta - \eta)], \\ E_Z &= \sum_{\eta=1}^{\zeta} [(\eta + 1)^{1-\alpha} - \eta^{1-\alpha}] [Z(\zeta + 1 - \eta) - Z(\zeta - \eta)]. \end{aligned}$$

Let us define  $\hat{Y}$  as the estimated state. Moreover, in estimated state  $\hat{Y}$ , we can derive the following Jacobian matrix of  $F(\bar{Y})$ :

$$J(\hat{Y}) = \begin{pmatrix} \mathcal{N}_{11}(\hat{Y}) & \mathcal{N}_{12}(\hat{Y}) & \mathcal{N}_{13}(\hat{Y}) & \mathcal{N}_{14}(\hat{Y}) \\ \mathcal{N}_{21}(\hat{Y}) & \mathcal{N}_{22}(\hat{Y}) & \mathcal{N}_{23}(\hat{Y}) & \mathcal{N}_{24}(\hat{Y}) \\ \mathcal{N}_{31}(\hat{Y}) & \mathcal{N}_{32}(\hat{Y}) & \mathcal{N}_{33}(\hat{Y}) & \mathcal{N}_{34}(\hat{Y}) \\ \mathcal{N}_{41}(\hat{Y}) & \mathcal{N}_{42}(\hat{Y}) & \mathcal{N}_{43}(\hat{Y}) & \mathcal{N}_{44}(\hat{Y}) \end{pmatrix},$$

where

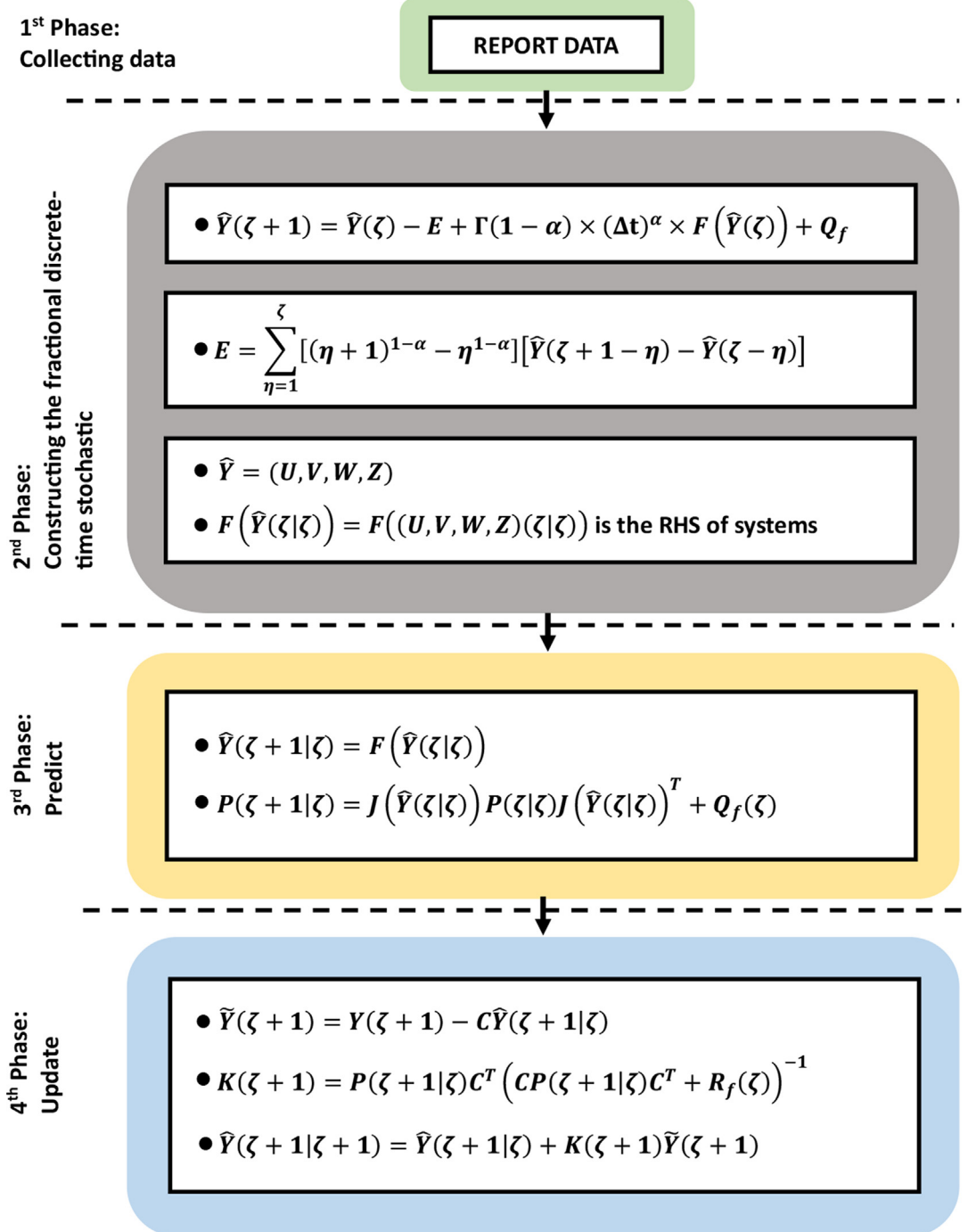


**Fig. 2.** Workflow of fractional extended Kalman filter (FracEKF) based on fractional discrete-time stochastic augmented CoVid-19 model consisting of state variables ( $U, V, W, Z$ ) and assumed parameters ( $\Lambda, \beta, \delta, \psi, r, \epsilon, d, \kappa$ ).

$$\begin{aligned}
 \mathcal{N}_{11} &= 1 + \Gamma(1 - \alpha) \times (\Delta t)^\alpha \times (-\beta \delta \widehat{V}^\zeta - \psi), \quad \mathcal{N}_{12} = -\Gamma(1 - \alpha) \times (\Delta t)^\alpha \times \beta \delta \widehat{U}^\zeta, \\
 \mathcal{N}_{13} &= 0, \quad \mathcal{N}_{14} = 0, \\
 \mathcal{N}_{21} &= \Gamma(1 - \alpha) \times (\Delta t)^\alpha \times \beta \delta \widehat{V}^\zeta, \quad \mathcal{N}_{22} = 1 + \Gamma(1 - \alpha) \times (\Delta t)^\alpha \times (\beta \delta \widehat{U}^\zeta - (r + \epsilon + \psi + d)), \\
 \mathcal{N}_{23} &= 0, \quad \mathcal{N}_{24} = 0, \\
 \mathcal{N}_{31} &= 0, \quad \mathcal{N}_{32} = \Gamma(1 - \alpha) \times (\Delta t)^\alpha \times \epsilon, \quad \mathcal{N}_{33} = 1 + v_3 - \Gamma(1 - \alpha) \times (\Delta t)^\alpha \times (\kappa + d + \psi), \\
 \mathcal{N}_{34} &= 0, \\
 \mathcal{N}_{41} &= 0, \quad \mathcal{N}_{42} = \Gamma(1 - \alpha) \times (\Delta t)^\alpha \times r, \quad \mathcal{N}_{43} = \Gamma(1 - \alpha) \times (\Delta t)^\alpha \times \kappa, \\
 \mathcal{N}_{44} &= 1 + v_4 - \Gamma(1 - \alpha) \times (\Delta t)^\alpha \times \psi.
 \end{aligned}$$

The fixed tuning parameters are the process covariance, the observation covariance, and the square identity matrix, which are defined as follows:

$$\begin{aligned}
 Q_f &= \begin{pmatrix} 10 & 0 & 0 & 0 \\ 0 & 10 & 0 & 0 \\ 0 & 0 & 10 & 0 \\ 0 & 0 & 0 & 5 \end{pmatrix}, \quad R_f = \begin{pmatrix} 100 & 0 & 0 & 0 \\ 0 & 10 & 0 & 0 \\ 0 & 0 & 10 & 0 \\ 0 & 0 & 0 & 1 \end{pmatrix}, \\
 C &= \begin{pmatrix} 1 & 0 & 0 & 0 \\ 0 & 1 & 0 & 0 \\ 0 & 0 & 1 & 0 \\ 0 & 0 & 0 & 1 \end{pmatrix},
 \end{aligned}$$

where the initial  $P$  is given by

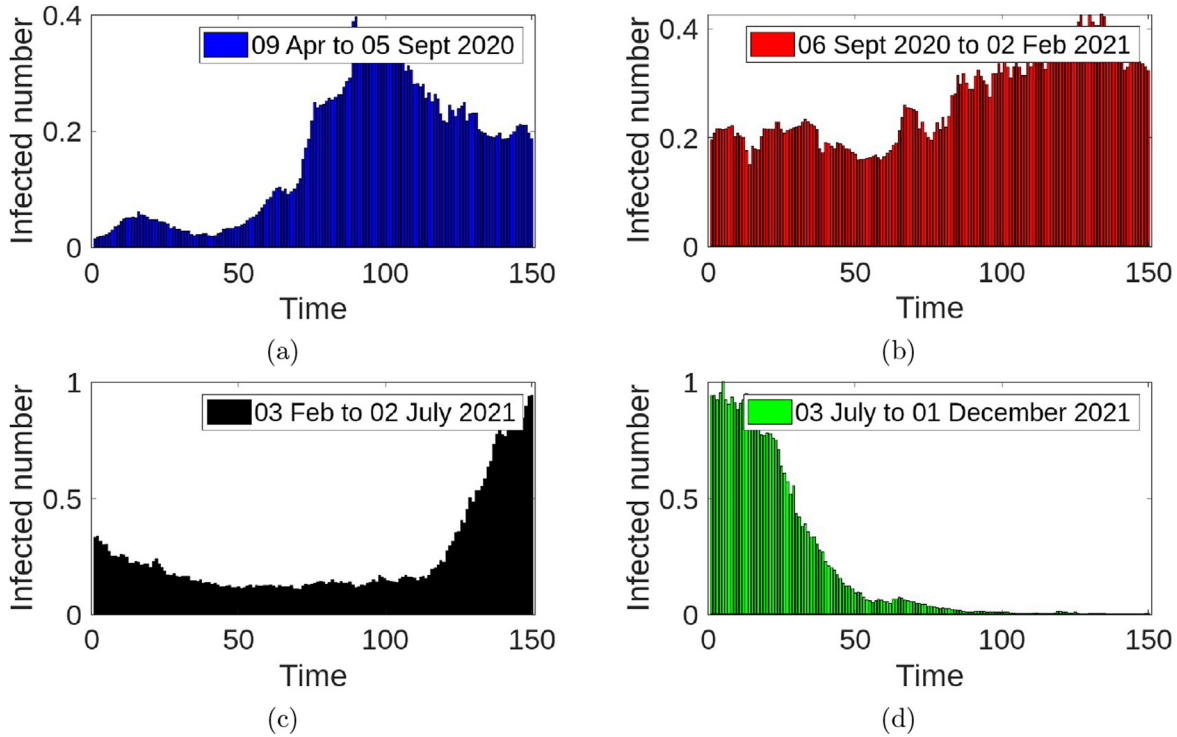


**Fig. 3.** Report data for individuals infected by CoVid-19 and consisting of phase  $\mathcal{T}_1$  (blue color), phase  $\mathcal{T}_2$  (red color), phase  $\mathcal{T}_3$  (black color), and phase  $\mathcal{T}_4$  (green color).

$$P = \begin{pmatrix} 1000 & 0 & 0 & 0 \\ 0 & 1000 & 0 & 0 \\ 0 & 0 & 1000 & 0 \\ 0 & 0 & 0 & 1000 \end{pmatrix}.$$

The accuracy of our model can be evaluated using the standard root mean square error (RMSE), normalized root mean square error (NRMSE), and mean absolute percentage error (MAPE), which are calculated as follows:

$$\begin{aligned} RMSE &= \sqrt{\frac{1}{M} \sum_{k=1}^M (\hat{H}_k - H_k)^2}, \quad NRMSE = \sqrt{\frac{1}{M} \sum_{k=1}^M \left(\frac{\hat{H}_k - H_k}{H_k}\right)^2}, \\ MAPE &= \frac{1}{M} \sum_{k=1}^M \frac{|\hat{H}_k - H_k|}{H_k} \times 100\%, \end{aligned} \quad (11)$$

where  $\hat{H}$  and  $H$  are the predicted results using FracEKF and the reported data (only infected individuals), respectively. The values of  $\hat{H}$  and  $H$  are represented as vectors consisting of 150 data points. The threshold of this proposed method is determined by 150 iterations, based on the quotient of 600 total data.

#### 4. Results and discussion

The endemic threshold can be analyzed by the sensitivity index based on the effect of various parameters, where all values of the sensitivity index are listed in Table 1 and visualized in Fig. 5a. Moreover, the sensitivity index can be obtained through the basic reproduction number  $\mathcal{R}_0$ , which is differentiable with respect to the parameter  $\pi$ :

$$\Gamma_{\pi}^{\mathcal{R}_0} = \frac{\partial \mathcal{R}_0}{\partial \pi} \times \frac{\pi}{\mathcal{R}_0}, \quad (12)$$

where

$$\pi = [\Lambda; \beta; \delta; \psi; r; \epsilon; d].$$

The highest sensitivity indices for each model parameter are achieved for  $\Lambda$  ( $\Gamma_{\Lambda}^{\mathcal{R}_0} = 1$ ),  $\beta$  ( $\Gamma_{\beta}^{\mathcal{R}_0} = 1$ ), and  $\delta$  ( $\Gamma_{\delta}^{\mathcal{R}_0} = 1$ ) for the birth rate, transmission rate, and physical distancing rate, respectively. This indicates that the birth, transmission, and physical distancing rates have the greatest impact on the number of individuals infected by CoVid-19, if there is contact directly between two or more individuals. The smallest sensitivity index is attained by  $\psi$  ( $\Gamma_{\psi}^{\mathcal{R}_0} = -1$ ), the natural mortality rate, which decreases the number of individuals infected by CoVid-19 by 100%. Moreover, the trans-

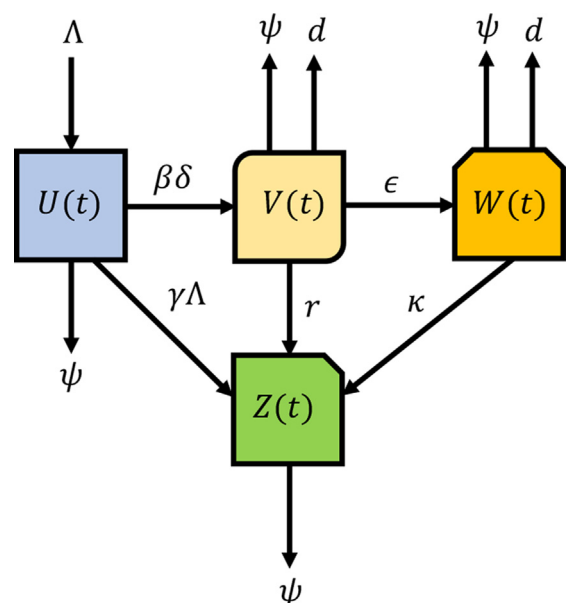


**Fig. 4.** 2nd compartment diagram of CoVid-19 model.

mision rate  $\beta$  and physical distancing rate  $\delta$  increase the number of individuals infected by CoVid-19 by 100% because they are directly proportional to the basic reproduction number  $\mathcal{R}_0$ . Similar values of the sensitivity index (44.10%) are attained by the isolation rate  $\epsilon$  and recovery rate of infected individuals  $r$ , which means that they have the same impact on decreasing the number of individuals infected by CoVid-19. According to Eq. (5), the recovery rate of isolated individuals  $\kappa$  has no effect on the basic reproduction number. Figs. 5e illustrate the influence of the isolation rate and infection

rate on the reproduction number and infected number, respectively (as in Fig. 5e, the red region indicates a higher number of infected individuals than the other regions, and indicates the highest basic reproduction number,  $\mathcal{R}_0 > 1$ , as in Fig. 5c). The infection rate is directly proportional and inversely proportional to the reproduction number and infected number, respectively. A smaller isolation rate leads to a greater number of infected individuals, while a higher isolation rate produces a greater number of infected individuals. This is in line with the basic reproduction number diagram, which shows

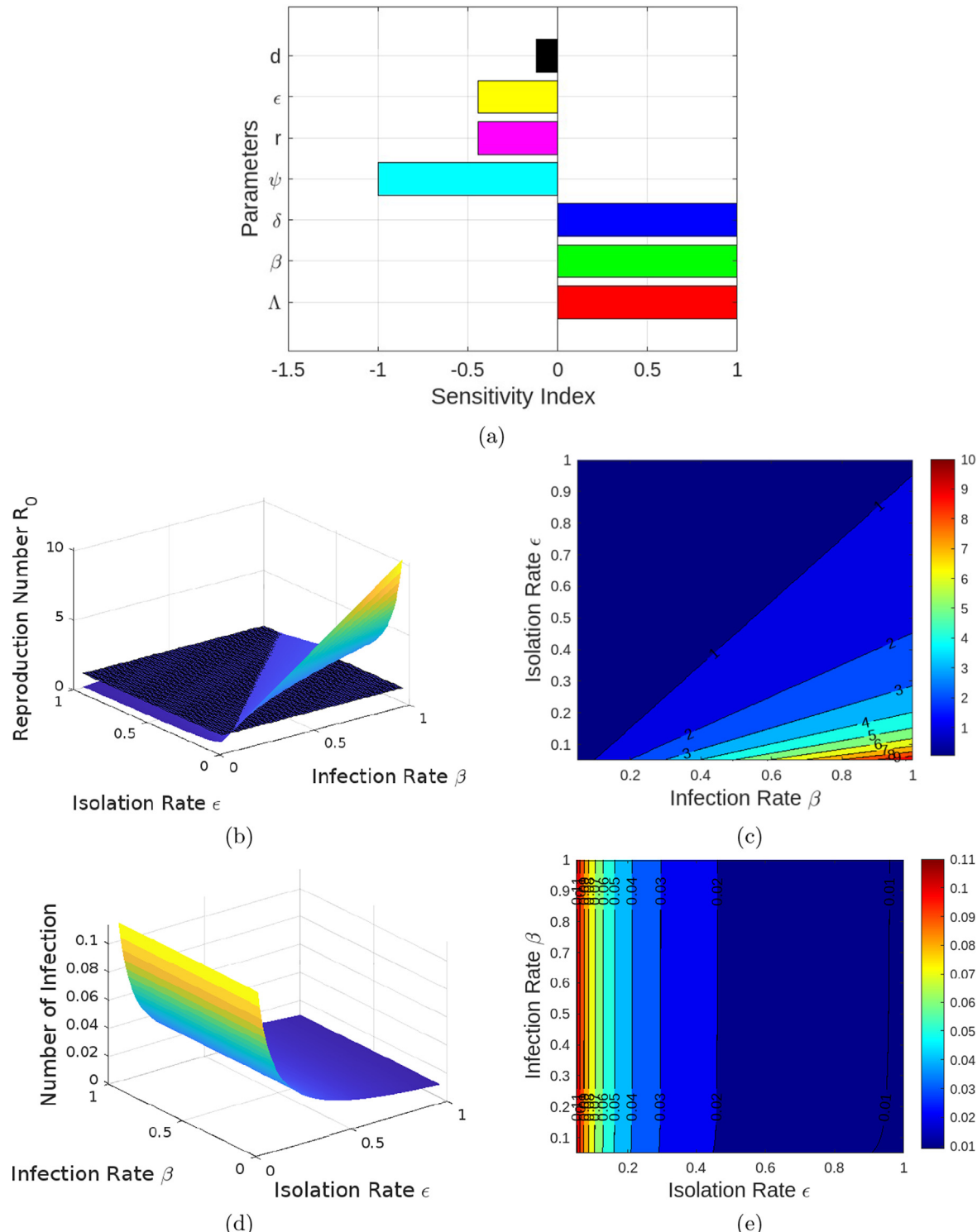


**Fig. 5.** (a) Partial rank correlation coefficient, (b)–(e) influence of isolation rate and infection rate on reproduction number and infected number.

that, if the isolation rate is increased, the spread of CoVid-19 will decrease ( $\mathcal{R}_0 < 1$ ), whereas if the isolation rate is small, CoVid-19 will spread ( $\mathcal{R}_0 > 1$ ). Moreover, the two diagrams showing the basic reproduction number  $\mathcal{R}_0(t)$  and number of infections  $V(t)$  are based on Eq. (5) and the equilibrium points for the endemic state in Theorem 2.3 considering the evolution of the infection rate  $\beta$  and the isolation rate  $\epsilon$ :

$$\mathcal{R}_0(t) = \frac{\Lambda\beta(t)\delta}{\psi(r + \epsilon(t) + \psi + d)}, \quad V(t) = \frac{\Lambda}{r + \epsilon(t) + \psi + d} - \frac{\psi}{\beta(t)\delta}.$$

In previous epidemiological models,<sup>9,26,40,49,53</sup> vaccination has a significant impact on decreasing the infection rate of the disease. Thus, we employ the vaccination rate  $\gamma$  in our fractional-order CoVid-19 model, as shown in Fig. 4, where the maximum rate of vaccination is 1 and the minimum rate of vaccination is 0. Table 2 presents the mean values of susceptible ( $U$ ), infected ( $V$ ), quarantined ( $W$ ), and recovered ( $Z$ ) individuals with and without vaccination. The results indicate that  $U$ ,  $V$ , and  $W$  decrease after vaccination, while  $Z$  increases. After incorporating vaccination into our fractional-order CoVid-19 model, we obtain the basic reproduction number  $\mathcal{R}_0 = \frac{\Lambda(1-\gamma)\beta\delta}{\psi(r+\epsilon+\psi+d)}$ , which is directly proportional to  $\gamma$ . The basic repro-

duction number before and after vaccination can be stated as  $\mathcal{R}_0(\text{with } \gamma) < \mathcal{R}_0(\text{without } \gamma)$ , which is in reasonable agreement with the results in Table 2, where vaccination reduces the number of susceptible, infected, and quarantined individuals, while increasing the number of recovered individuals. According to the prediction results for our fractional-order CoVid-19 model with the report data using FracEKF in Table 3, vaccination can reduce the mean infection number for CoVid-19, even though the difference before and after vaccination is small, namely 0.004, 0.0028, and 0.002 for  $\alpha = 0.01$ ,  $\alpha = 0.05$ , and  $\alpha = 0.09$ , respectively. Moreover, the mean values in Fig. 6 are based on the predictive results of the infection number for CoVid-19 in Semarang, Indonesia, using FracEKF with eight combinations (P1–P8) of the physical distancing rate ( $\delta$ ), isolation rate ( $\epsilon$ ), and vaccination rate ( $\gamma$ ). Specifically, P1 = [ $\gamma = 0, \delta = 0, \epsilon = 0$ ], P2 = [ $\gamma = 0, \delta = 0.4, \epsilon = 0$ ], P3 = [ $\gamma = 0.5, \delta = 0, \epsilon = 0$ ], P4 = [ $\gamma = 0, \delta = 0, \epsilon = 0.03$ ], P5 = [ $\gamma = 0.5, \delta = 0.4, \epsilon = 0$ ], P6 = [ $\gamma = 0.5, \delta = 0, \epsilon = 0.03$ ], P7 = [ $\gamma = 0, \delta = 0.4, \epsilon = 0.03$ ], and P8 = [ $\gamma = 0.5, \delta = 0.4, \epsilon = 0.03$ ]. Combination P6 gives the smallest infection number caused by CoVid-19 after employing vaccination ( $\gamma = 0.5$ ), isolation ( $\epsilon = 0.03$ ), and the maximum physical distancing ( $\delta = 0$ ). The highest infection number is attained by combination P1, which employs no vaccination ( $\gamma = 0$ ) or isolation

**Table 2**

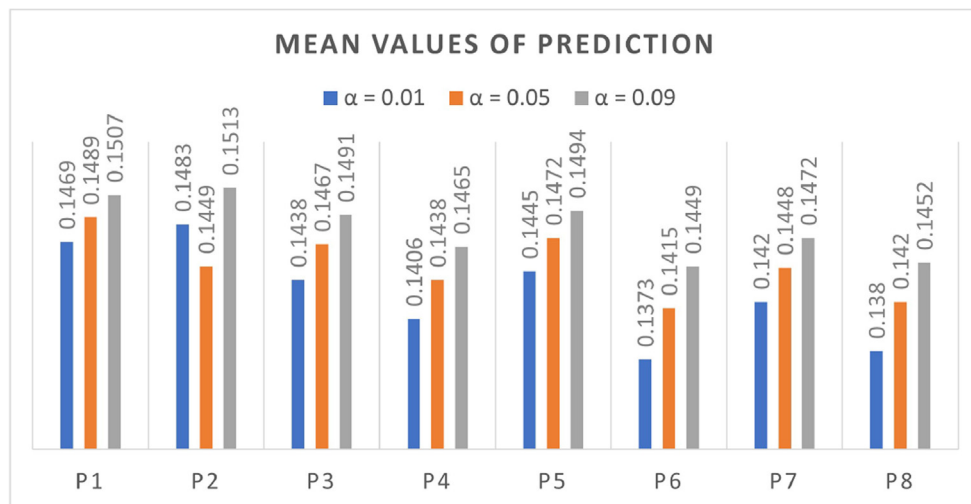
Mean values of susceptible, infected, quarantined, and recovered individuals for each fractional-order  $\alpha$  with and without vaccination ( $\gamma$ ).

Without Vaccination ( $\gamma = 0$ )											
$\alpha = 0.75$				$\alpha = 0.8$				$\alpha = 0.85$			
$U$	$V$	$W$	$Z$	$U$	$V$	$W$	$Z$	$U$	$V$	$W$	$Z$
2.84	1.23	0.05	5.18	3.01	1.07	0.05	5.78	3.22	0.95	0.04	6.4351
With Vaccination ( $\gamma = 0.5$ )											
$\alpha = 0.75$				$\alpha = 0.8$				$\alpha = 0.85$			
$U$	$V$	$W$	$Z$	$U$	$V$	$W$	$Z$	$U$	$V$	$W$	$Z$
2.31	1.00	0.04	5.95	2.41	0.82	0.03	6.65	2.59	0.66	0.03	7.38

**Table 3**

Mean values of reported CoVid-19 data for infected individuals ( $V$ ) using FracEKF for each fractional-order  $\alpha$  with and without vaccination ( $\gamma$ ).

Without Vaccination ( $\gamma = 0$ )			With Vaccination ( $\gamma = 0.5$ )		
$\alpha = 0.01$	$\alpha = 0.05$	$\alpha = 0.09$	$\alpha = 0.01$	$\alpha = 0.05$	$\alpha = 0.09$
0.1420	0.1448	0.1472	0.1380	0.1420	0.1452

**Fig. 6.** Mean values of individuals infected by CoVid-19  $V$  for eight combinations (P1–P8) of physical distancing ( $\delta$ ), isolation rate ( $\epsilon$ ), and vaccination ( $\gamma$ ).

( $\epsilon = 0$ ), but does employ the maximum physical distancing ( $\delta = 0$ ). Thus, we can conclude that implementing physical distancing, isolation, and vaccination at once guarantees the smallest number of infected individuals, as in the results for P6 (Fig. 6).

The influence of the memory effect (fractional-orders of  $\alpha = 0.75$ ,  $\alpha = 0.8$ ,  $\alpha = 0.85$ , and  $\alpha = 0.9$ ) is illustrated in Fig. 8a–8d for the endemic state ( $\mathcal{R}_0 > 1$ ) and Fig. 7a–7d for the disease-free state ( $\mathcal{R}_0 < 1$ ). In the disease-free state ( $\mathcal{R}_0 < 1$ ), the profiles of infected and quarantined individuals have steeper slopes than

in the endemic state ( $\mathcal{R}_0 > 1$ ). The susceptible number when  $\mathcal{R}_0 < 1$  is higher than when  $\mathcal{R}_0 > 1$ , reflecting the recovered number of individuals being lower in the former case. The quarantined number when  $\mathcal{R}_0 < 1$  approaches zero because this is directly proportional to the infected number in the disease-free state, which also approaches zero, i.e., decreasing the infected number reduces the quarantined number. According to the values for all parameters in Table 1, the disease-free state ( $\mathcal{R}_0 < 1$ ) is achieved when  $\delta = 0.04$  and  $\epsilon = 0.9$ , giving basic reproduction numbers of

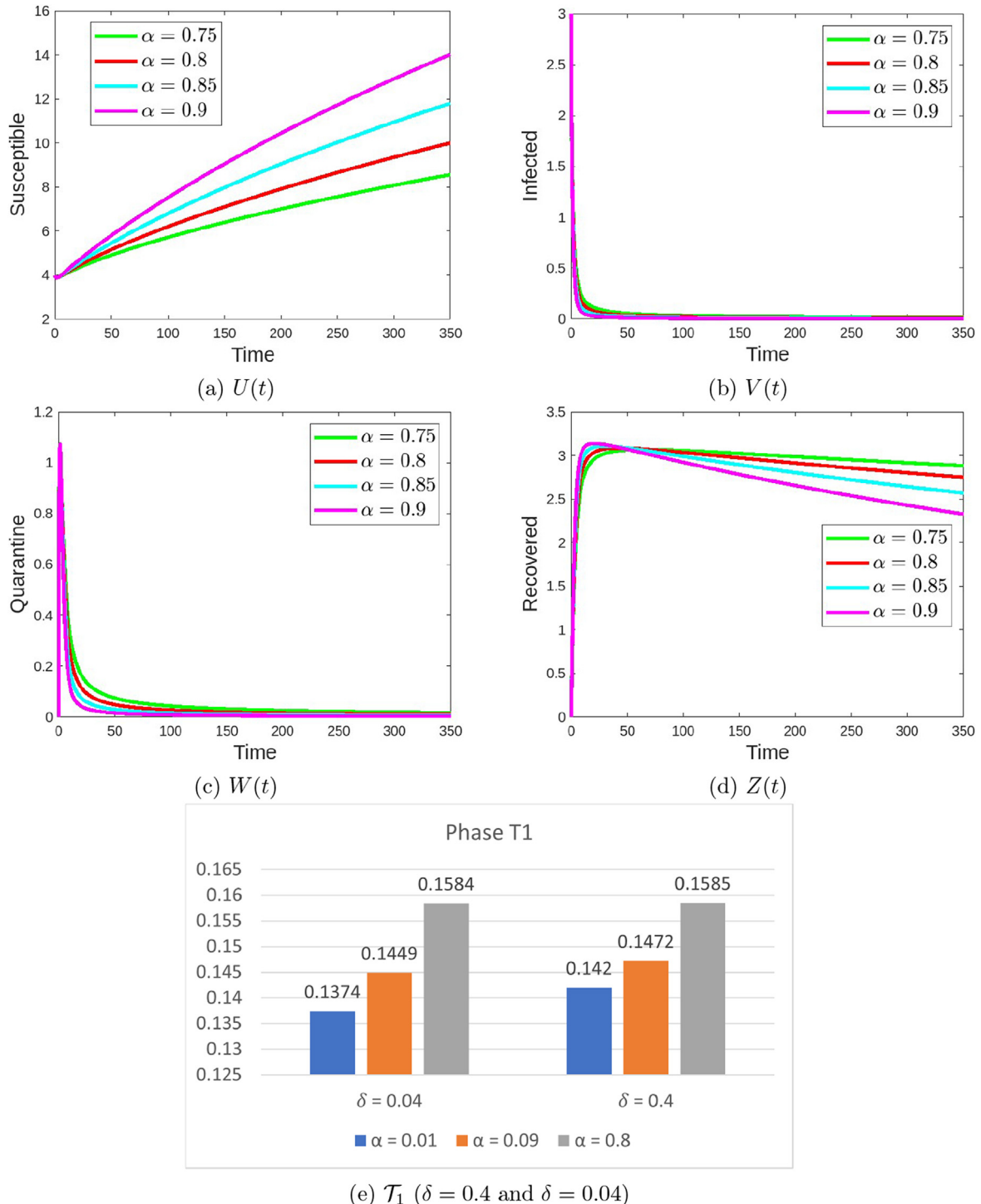


**Fig. 7.** (a)–(d) Dynamics of fractional CoVid-19 model for the basic reproduction number  $\mathcal{R}_0 < 1$  and (e) mean values of infected individuals with physical distancing  $\delta = 0.4$  ( $\mathcal{R}_0 > 1$ ) and  $\delta = 0.04$  ( $\mathcal{R}_0 < 1$ ) for phase  $\mathcal{T}_1$ .

$\mathcal{R}_0 = 0.9344$  and  $\mathcal{R}_0 = 0.8751$ , respectively. Based on these results, the isolation rate is more effective than physical distancing in reducing the number of individuals infected by CoVid-19. If we compare this with the prediction results using FracEKF, as shown in Figs. eeee7–10, we can conclude that changes in the physical distancing rate (from  $\delta = 0.4$  to  $\delta = 0.04$ ) do not have a significant impact (small difference when increasing the fractional-order  $\alpha$ ). These results are different from those for the isolation rate (increasing from  $\epsilon = 0.03$  to  $\epsilon = 0.9$ ), which has a significant impact

(significant difference when increasing the fractional-order  $\alpha$ ), as in Fig. 9a–9d and Fig. 10a–10d for all phases ( $\mathcal{T}_1, \mathcal{T}_2, \mathcal{T}_3, \mathcal{T}_4$ ). Theoretically, this makes sense because isolation prevents any interaction with other individuals; in this case, individuals who are self-isolating should not leave their homes, even to go for a walk alone (in practice, they are only allowed to leave their homes for emergencies). This is different from physical distancing, where there is still the opportunity to leave the house and interact with other individuals, although contact is limited to a certain distance. More-

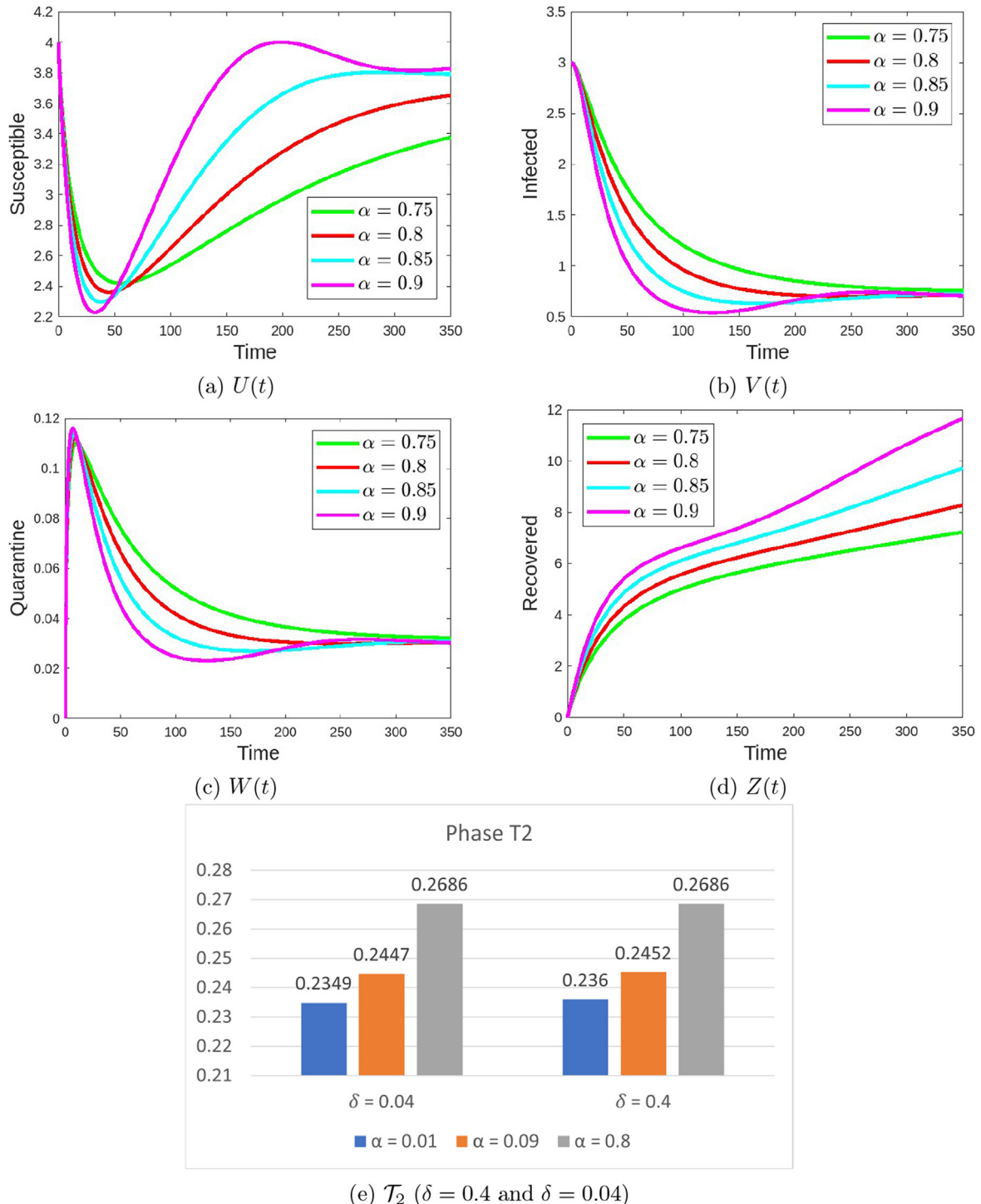


**Fig. 8.** (a)–(d) Dynamics of fractional CoVid-19 model for the basic reproduction number  $\mathcal{R}_0 > 1$  and (e) mean values of infected individuals with physical distancing  $\delta = 0.4$  ( $\mathcal{R}_0 > 1$ ) and  $\delta = 0.04$  ( $\mathcal{R}_0 < 1$ ) for phase  $\mathcal{T}_2$ .

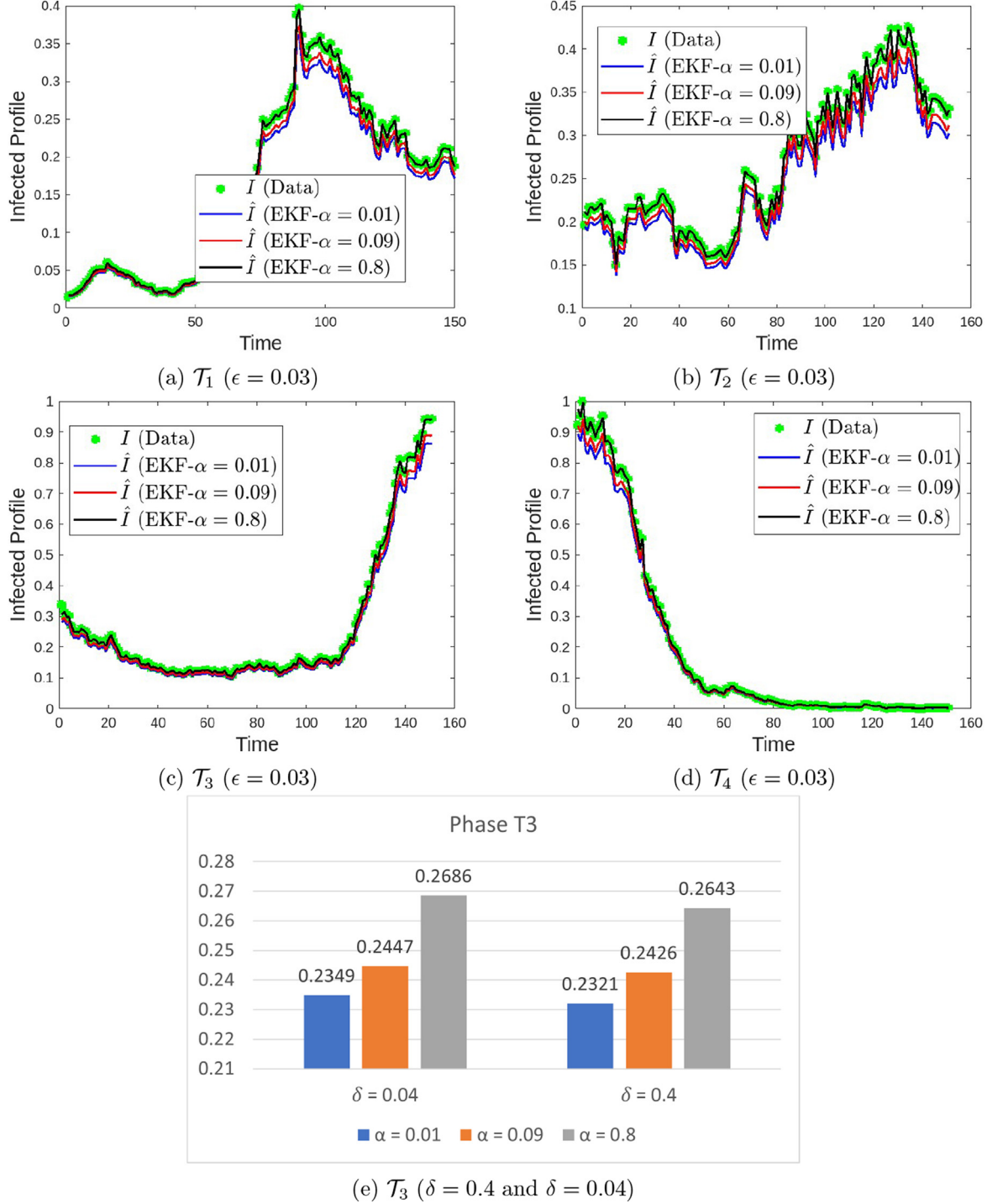


**Fig. 9.** Prediction results of our fractional CoVid-19 model using FracEKF for (a)–(d) the isolation rate  $\epsilon = 0.03$  ( $\mathcal{R}_0 > 1$ ) and (e) mean values of infected individuals with physical distancing  $\delta = 0.4$  ( $\mathcal{R}_0 > 1$ ) and  $\delta = 0.04$  ( $\mathcal{R}_0 < 1$ ) for phase  $\mathcal{T}_3$ .

over, as the fractional-order increases (from  $\alpha = 0.75$  to  $\alpha = 0.9$ ), less time is required to reach stable numbers of infected and quarantined individuals, and more time is required to reach stable numbers of susceptible and quarantined individuals (for both  $\mathcal{R}_0 < 1$  and  $\mathcal{R}_0 > 1$ ).

The reported CoVid-19 data (from April 9, 2020 to December 1, 2021) are presented in Fig. 3. We further divide the data into four phases, which are represented as  $\mathcal{T}_1, \mathcal{T}_2, \mathcal{T}_3$ , and  $\mathcal{T}_4$  for April 9 to September 5, 2020 (Fig. 3a), September 6, 2020 to February 2, 2021 (Fig. 3b), February 3 to July 2, 2021 (Fig. 3c), and July 3 to Decem-

ber 1 2021 (Fig. 3d), respectively. Fig. 3a reaches a peak of 0.3967 (976 infected individuals) on July 7, 2020, Fig. 3b reaches a peak of 0.4260 (1048 infected individuals) on January 17, 2021, Fig. 3c reaches a peak of 0.9435 (2321 infected individuals) on July 2, 2021, and Fig. 3d reaches a peak of 1 (2460 infected individuals) on July 7, 2021. Applying FracEKF to our fractional-order model and the reported CoVid-19 data illustrates the accuracy in terms of RMSE, NRMSE, and MAPE. As in Fig. 9a–9d and Fig. 10a–10d, the infected profiles exhibit similar patterns for each fractional-order. The trend in the number of infected individuals for the

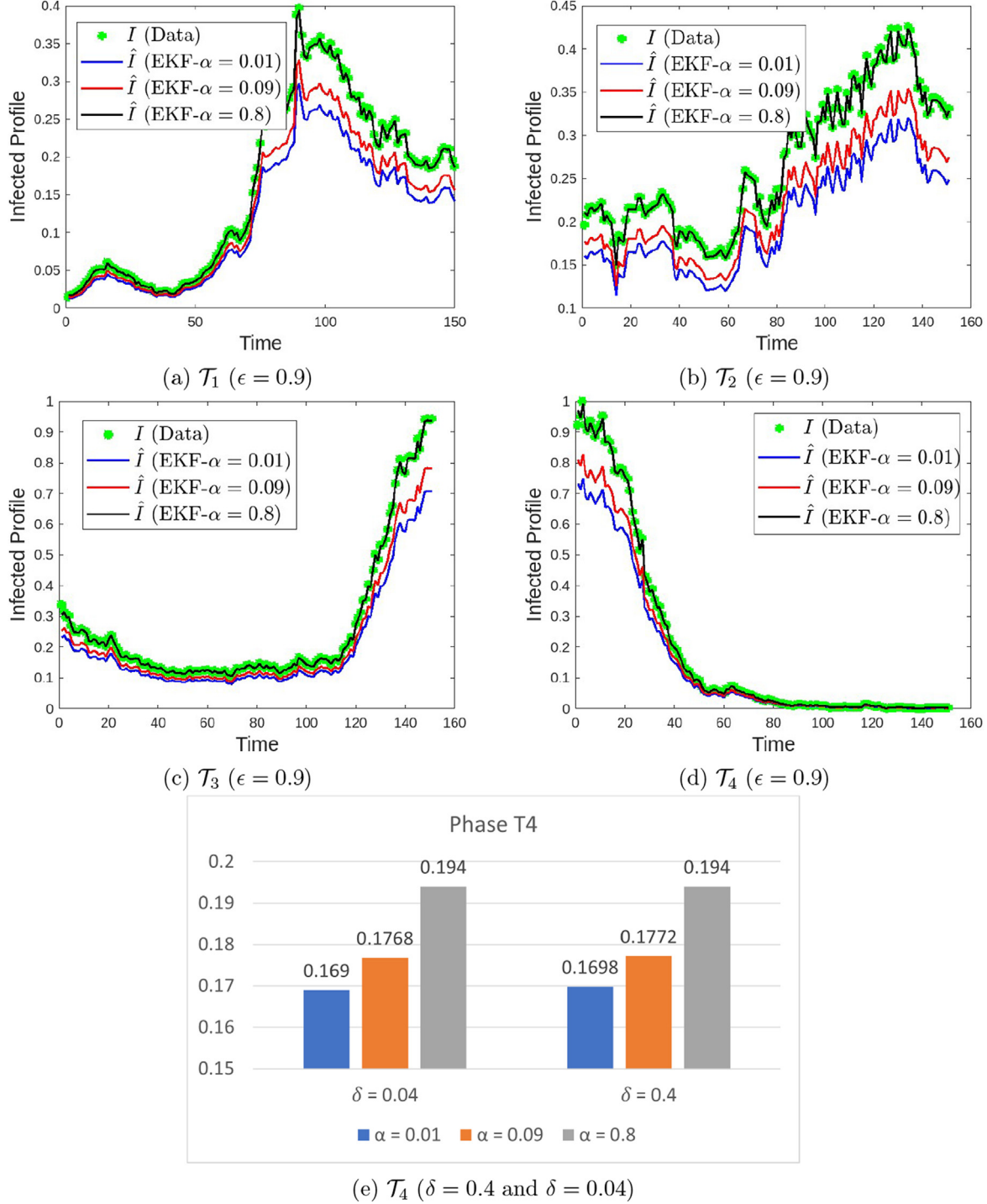


**Fig. 10.** Prediction results of our fractional CoVid-19 model using FracEKF for (a)–(d) the isolation rate  $\epsilon = 0.9$  ( $\mathcal{R}_0 < 1$ ) and (e) mean values of infected individuals with physical distancing  $\delta = 0.4$  ( $\mathcal{R}_0 > 1$ ) and  $\delta = 0.04$  ( $\mathcal{R}_0 < 1$ ) for phase  $\mathcal{T}_4$ .

disease-free state ( $\mathcal{R}_0 < 1$  and  $\epsilon = 0.9$ ) has a steeper slope than that for the endemic state ( $\mathcal{R}_0 > 1$  and  $\epsilon = 0.03$ ). We can conclude that increasing the isolation rate ( $\epsilon$ ) significantly reduces the number of infected individuals. Moreover, Fig. 9a–9d and Fig. 10a–10d exhibit the same pattern in terms of the value at the peak point increasing as the fractional-order  $\alpha$  increases (black line ( $\alpha = 0.8$ ) is closest to the reported data, blue line ( $\alpha = 0.01$ ) is farthest from the reported data).

The RMSE, NRMSE, and MAPE for all phases ( $\mathcal{T}_1, \mathcal{T}_2, \mathcal{T}_3$ , and  $\mathcal{T}_4$ ) with respect to the fractional-order  $\alpha$  ( $\alpha = 0.01, \alpha = 0.05$ , and  $\alpha = 0.09$ ) are represented in Fig. 16 and Tables 4, 5 for various  $Q_f$  and  $R_f$ . We can conclude that a higher fractional-order produces a higher level of accuracy (predictive results using FracEKF are closer to the reported data). The computation time of FracEKF for each phase is denoted as ( $C_{\text{FracEKF}}$ ). The computation times for each phase are as follows: for phase  $\mathcal{T}_1, C_{\text{FracEKF}}(\alpha =$

**Table 4**Accuracy values for various  $Q_f$  with fixed  $R_f$ .

Varying $Q_f$ and Fixed $R_f$	Accuracy	phase $\mathcal{T}_1$		
		$\alpha = 0.01$	$\alpha = 0.05$	$\alpha = 0.09$
$Q_{f1}$ (Normal)	RMSE	0.0167	0.0136	0.0111
	NRMSE	0.1051	0.0858	0.0701
	MAPE	8.53%	6.99%	5.74%
$Q_{f2}$ (2 Times)	RMSE	0.0098	0.0080	0.0066
	NRMSE	0.0620	0.0506	0.0413
	MAPE	5.09%	4.18%	3.44%
$Q_{f3}$ (3 Times)	RMSE	0.0071	0.0058	0.0047
	NRMSE	0.0445	0.0363	0.0297
	MAPE	3.69%	3.04%	2.52%
phase $\mathcal{T}_2$				
$Q_{f1}$ (Normal)	RMSE	0.0238	0.0194	0.0159
	NRMSE	0.0883	0.0721	0.0589
	MAPE	8.41%	6.87%	5.62%
$Q_{f2}$ (2 Times)	RMSE	0.0140	0.0115	0.0094
	NRMSE	0.0521	0.0426	0.0349
	MAPE	4.98%	4.07%	3.34%
$Q_{f3}$ (3 Times)	RMSE	0.0101	0.0083	0.0068
	NRMSE	0.0375	0.0307	0.0252
	MAPE	3.59%	2.94%	2.41%
phase $\mathcal{T}_3$				
$Q_{f1}$ (Normal)	RMSE	0.0301	0.0246	0.0202
	NRMSE	0.1133	0.0928	0.0762
	MAPE	8.54%	6.98%	5.72%
$Q_{f2}$ (2 Times)	RMSE	0.0179	0.0148	0.0122
	NRMSE	0.0676	0.0556	0.0459
	MAPE	5.06%	4.14%	3.40%
$Q_{f3}$ (3 Times)	RMSE	0.0131	0.0108	0.0090
	NRMSE	0.0492	0.0407	0.0339
	MAPE	3.65%	2.99%	2.46%
phase $\mathcal{T}_4$				
$Q_{f1}$ (Normal)	RMSE	0.0301	0.0245	0.0199
	NRMSE	0.1549	0.1261	0.1027
	MAPE	8.25%	6.73%	5.48%
$Q_{f2}$ (2 Times)	RMSE	0.0176	0.0144	0.0118
	NRMSE	0.0909	0.0743	0.0610
	MAPE	4.85%	3.95%	3.23%
$Q_{f3}$ (3 Times)	RMSE	0.0127	0.0105	0.0087
	NRMSE	0.0656	0.0541	0.0450
	MAPE	3.48%	2.84%	2.31%

$0.01) = 33.541488$ ,  $C_{FracEKF}(\alpha = 0.05) = 33.565220$ , and  $C_{FracEKF}(\alpha = 0.09) = 33.820377$ ; for phase  $\mathcal{T}_2$ ,  $C_{FracEKF}(\alpha = 0.01) = 34.473412$ ,  $C_{FracEKF}(\alpha = 0.05) = 34.255812$ , and  $C_{FracEKF}(\alpha = 0.09) = 34.166675$ ; for phase  $\mathcal{T}_3$ ,  $C_{FracEKF}(\alpha = 0.01) = 34.521463$ ,  $C_{FracEKF}(\alpha = 0.05) = 34.375349$ , and  $C_{FracEKF}(\alpha = 0.09) = 33.932779$ ; and for phase  $\mathcal{T}_4$ ,  $C_{FracEKF}(\alpha = 0.01) = 34.420729$ ,  $C_{FracEKF}(\alpha = 0.05) = 33.531188$ , and  $C_{FracEKF}(\alpha = 0.09) = 34.000153$ . The accuracy with various  $Q_f$  is listed in **Table 4** and the related error values are shown in **Figs. 11 and 12**. Higher values of  $Q_f$  produce smaller errors (the results are closer to the reported data for each fractional-order  $\alpha$ ), whereas higher values of  $R_f$  give higher errors (the results are farther away from the reported data for each fractional-order  $\alpha$ ), as shown in **Figs. 13 and 14**; more detailed accuracy values are listed in **Table 5**. According to the profiles of RMSE, NRMSE, and MAPE in **Fig. 15**, the errors increase when  $R_{f1}$ ,  $R_{f2}$ , and  $R_{f3}$  increase, and decrease when  $Q_{f1}$ ,  $Q_{f2}$ , and  $Q_{f3}$  increase. The values of RMSE, NRMSE and MAPE decrease when  $\alpha_1$ ,  $\alpha_2$ , and  $\alpha_3$  increase, as shown in **Fig. 16**. Mathematically, this can be expressed as follows:  $(Q_{f1}, Q_{f2}, Q_{f3}) \sim (\frac{1}{RMSE}, \frac{1}{NRMSE}, \frac{1}{MAPE})$ ,  $(R_{f1}, R_{f2}, R_{f3}) \sim (RMSE, NRMSE, MAPE)$ , and  $(\alpha_1, \alpha_2, \alpha_3) \sim (\frac{1}{RMSE}, \frac{1}{NRMSE}, \frac{1}{MAPE})$ , where  $Q_f$  and  $\alpha$  are inversely proportional to RMSE, NRMSE, and MAPE, and  $R_f$  is directly proportional to RMSE, NRMSE, and MAPE.

Based on the values of RMSE, NRMSE, and MAPE when using FracEKF, the results are highly significant for each fractional-order. Moreover, a higher fractional-order gives the most accurate

results (accuracy value for  $\alpha_3 = 0.8$  is higher than with  $\alpha_1 = 0.01$  and  $\alpha_2 = 0.09$ ). The errors when using  $\alpha_3 = 0.8$  are as follows:

[RMSE; NRMSE; MAPE] = [5.2046e-04; 0.0033; 0.36%] for phase  $\mathcal{T}_1$ ,

[RMSE; NRMSE; MAPE] = [0.0014; 0.0053; 0.26%] for phase  $\mathcal{T}_2$ ,

[RMSE; NRMSE; MAPE] = [0.0027; 0.0101; 0.27%] for phase  $\mathcal{T}_3$ ,

[RMSE; NRMSE; MAPE] = [0.0042; 0.0216; 0.27%] for phase  $\mathcal{T}_4$ .

## 5. Conclusions

This paper has examined a fractional-order CoVid-19 model. The results show that the reproduction number is directly proportional to the infection number and inversely proportional to the isolation rate. Varying the isolation rate provides meaningful results for the profiles of our CoVid-19 model for each unit of time, although the effect of physical distancing is not as significant as the effect of isolation. When the isolation rate increases, the infected number decreases, the susceptible number increases, the quarantined number decreases sharply, and the recovered number decreases. Moreover, the effect of vaccination was also considered in our CoVid-19 model. The combination of physical distancing, isolation rate, and vaccination has a significant impact on reducing the number of infected individuals. Analysis of dynamical systems was applied to understand the characteristics of our model, such as the boundedness and non-negativity, the existence of equilibrium

**Table 5**Accuracy values for various  $R_f$  with fixed  $Q_f$ .

		phase $\mathcal{T}_1$		
Varying $R_f$ and Fixed $Q_f$	Accuracy	$\alpha = 0.01$	$\alpha = 0.05$	$\alpha = 0.09$
$R_{f1}$ (Normal)	RMSE	0.0167	0.0136	0.0111
	NRMSE	0.1051	0.0858	0.0701
	MAPE	8.53%	6.99%	5.74%
$R_{f2}$ (2 Times)	RMSE	0.0270	0.0221	0.0180
	NRMSE	0.1700	0.1389	0.1136
	MAPE	13.70%	11.23%	9.21%
$R_{f3}$ (3 Times)	RMSE	0.0350	0.0287	0.0235
	NRMSE	0.2204	0.1806	0.1478
	MAPE	17.73%	14.55%	11.94%
phase $\mathcal{T}_2$				
$R_{f1}$ (Normal)	RMSE	0.0238	0.0194	0.0159
	NRMSE	0.0883	0.0721	0.0589
	MAPE	8.41%	6.87%	5.62%
$R_{f2}$ (2 Times)	RMSE	0.0384	0.0314	0.0257
	NRMSE	0.1426	0.1166	0.0954
	MAPE	13.62%	11.14%	9.10%
$R_{f3}$ (3 Times)	RMSE	0.0498	0.0408	0.0334
	NRMSE	0.1848	0.1515	0.1242
	MAPE	17.66%	14.48%	11.86%
phase $\mathcal{T}_3$				
$R_{f1}$ (Normal)	RMSE	0.0301	0.0246	0.0202
	NRMSE	0.1133	0.0928	0.0762
	MAPE	8.54%	6.98%	5.72%
$R_{f2}$ (2 Times)	RMSE	0.0483	0.0396	0.0325
	NRMSE	0.1822	0.1492	0.1223
	MAPE	13.77%	11.27%	9.23%
$R_{f3}$ (3 Times)	RMSE	0.0625	0.0513	0.0421
	NRMSE	0.2357	0.1935	0.1587
	MAPE	17.83%	14.63%	11.99%
phase $\mathcal{T}_4$				
$R_{f1}$ (Normal)	RMSE	0.0301	0.0245	0.0199
	NRMSE	0.1549	0.1261	0.1027
	MAPE	8.25%	6.73%	5.48%
$R_{f2}$ (2 Times)	RMSE	0.0489	0.0399	0.0325
	NRMSE	0.2520	0.2055	0.1675
	MAPE	13.34%	10.91%	8.91%
$R_{f3}$ (3 Times)	RMSE	0.0636	0.0520	0.0425
	NRMSE	0.3276	0.2679	0.2188
	MAPE	17.25%	14.16%	11.60%

points, the existence and uniqueness of solutions, and the local and global stability.

The highest sensitivity indices for each model parameter are achieved by varying  $\Lambda$  ( $\Gamma^{\mathcal{R}_0} = 1$ ),  $\beta$  ( $\Gamma^{\mathcal{R}_0} = 1$ ), and  $\delta$  ( $\Gamma^{\mathcal{R}_0} = 1$ ), which correspond to the birth rate, infection rate, and physical distancing rate, respectively. This indicates that the birth, infection, and physical distance rates have the greatest impact on increasing the number of individuals infected by CoVid-19, if there is contact directly between two or more individuals. The smallest sensitivity index is only attained by  $\psi$  ( $\Gamma^{\mathcal{R}_0} = -1$ ), the natural mortality rate, which has an impact of 100% in terms of reducing the number of individuals infected by CoVid-19. Moreover, the infection rate  $\beta$  and physical distancing rate  $\delta$  have an impact of 100% on increasing the number of individuals infected by CoVid-19 because they are directly proportional to the basic reproduction number,  $\mathcal{R}_0$ . Similar values of the sensitivity index (44.10%) are attained by the isolation rate  $\epsilon$  and recovery rate of infected individuals  $r$ , which means that they have the same impact on degrading the number of individuals infected by CoVid-19. In the disease-free state ( $\mathcal{R}_0 < 1$ ), the profiles of infected and quarantined individuals are steeper than those in endemic state ( $\mathcal{R}_0 > 1$ ). The number of susceptible individuals when  $\mathcal{R}_0 < 1$  is higher than that when  $\mathcal{R}_0 > 1$ , reflecting that the number of recovered individuals is lower for  $\mathcal{R}_0 < 1$ . The number of quarantined individuals in the case where  $\mathcal{R}_0 < 1$  approaches zero because this is directly propor-

tional to the number of infected individuals for  $\mathcal{R}_0 < 1$ , which also approaches zero, i.e., decreasing the number of infected individuals reduces the number of quarantined individuals in this case.

Higher values of  $Q_f$  were observed to produce smaller error values (results closer to the reported data for all fractional-orders  $\alpha$ ), whereas higher values of  $R_f$  gave higher errors (results farther from the reported data for all fractional-orders  $\alpha$ ). The profiles of RMSE, NRMSE, and MAPE can be mathematically stated as follows:  $(Q_{f1}, Q_{f2}, Q_{f3}) \sim (\frac{1}{RMSE}, \frac{1}{NRMSE}, \frac{1}{MAPE})$ ,  $(R_{f1}, R_{f2}, R_{f3}) \sim (RMSE, NRMSE, MAPE)$ , and  $(\alpha_1, \alpha_2, \alpha_3) \sim (\frac{1}{RMSE}, \frac{1}{NRMSE}, \frac{1}{MAPE})$ , where  $Q_f$  and  $\alpha$  are inversely proportional to RMSE, NRMSE, and MAPE, and  $R_f$  is directly proportional to RMSE, NRMSE, and MAPE.

Based on the results presented in this paper (accuracy of predictions using FracEKF, effectiveness of isolation, physical distancing, and vaccination), our model is sufficiently robust to predict the spread of CoVid-19. We can determine which combinations of the isolation rate, physical distancing rate, and vaccination rate are more effective in reducing the number of infected individuals, as illustrated in Fig. 6. Thus, our model can be used as an intervention strategy in combating CoVid-19. As a future study, we recommend adding the effects of a saturated incidence rate and temporary immunity to our model for three cases, namely a time-fractional order or space-fractional order with the Laplace operator approach, or a combination of both.

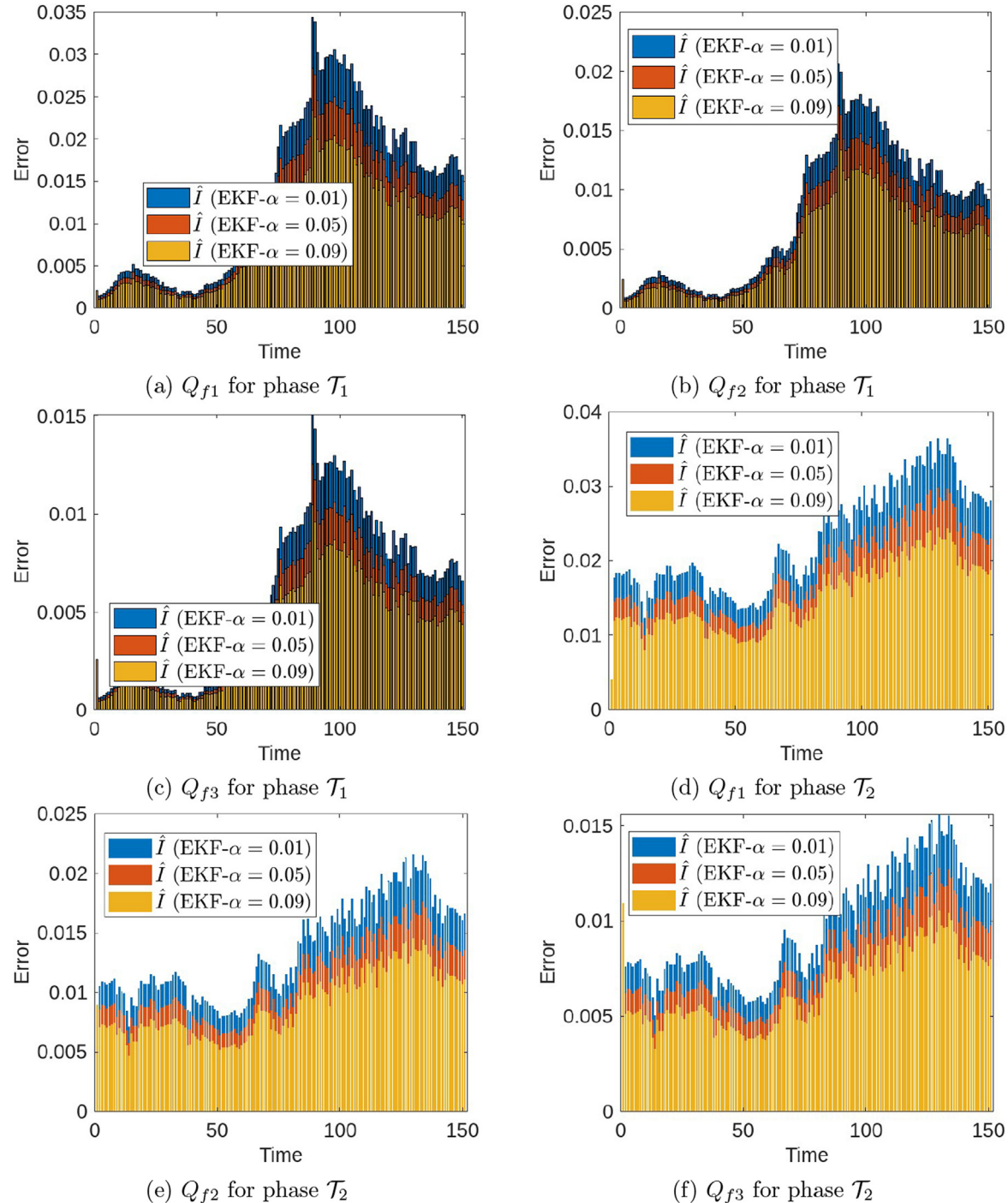


**Fig. 11.** Error values between predictions and reported data for various  $Q_f$ :  $Q_{f1} = (10; 10; 10; 5)$ ,  $Q_{f2} = (20; 20; 20; 10)$ , and  $Q_{f3} = (30; 30; 30; 15)$  in phases  $\mathcal{T}_1, \mathcal{T}_2$ .

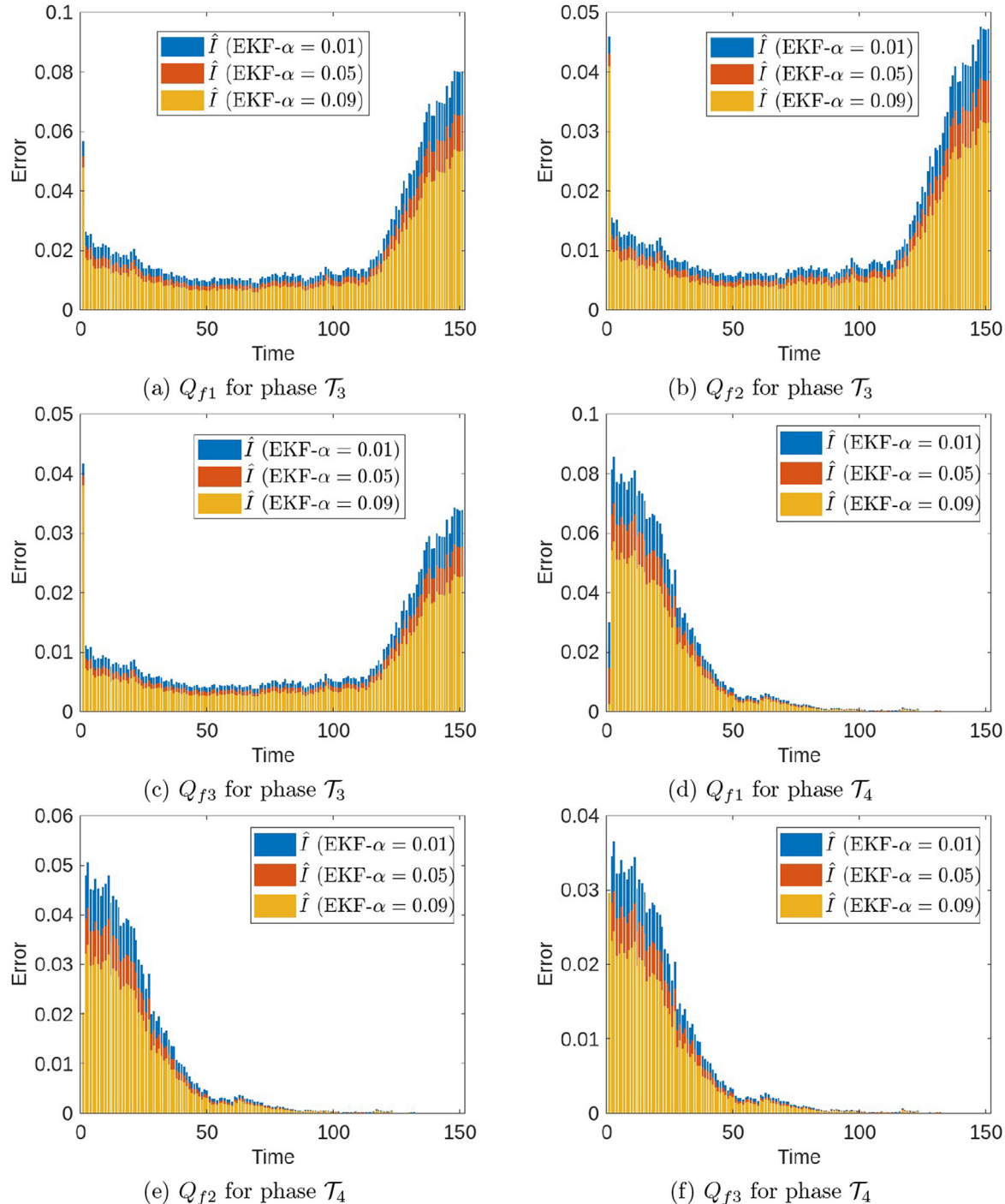


**Fig. 12.** Error values between predictions and reported data for various  $Q_f : Q_{f1} = (10; 10; 10; 5)$ ,  $Q_{f2} = (20; 20; 20; 10)$ , and  $Q_{f3} = (30; 30; 30; 15)$  in phases  $\mathcal{T}_3, \mathcal{T}_4$ .

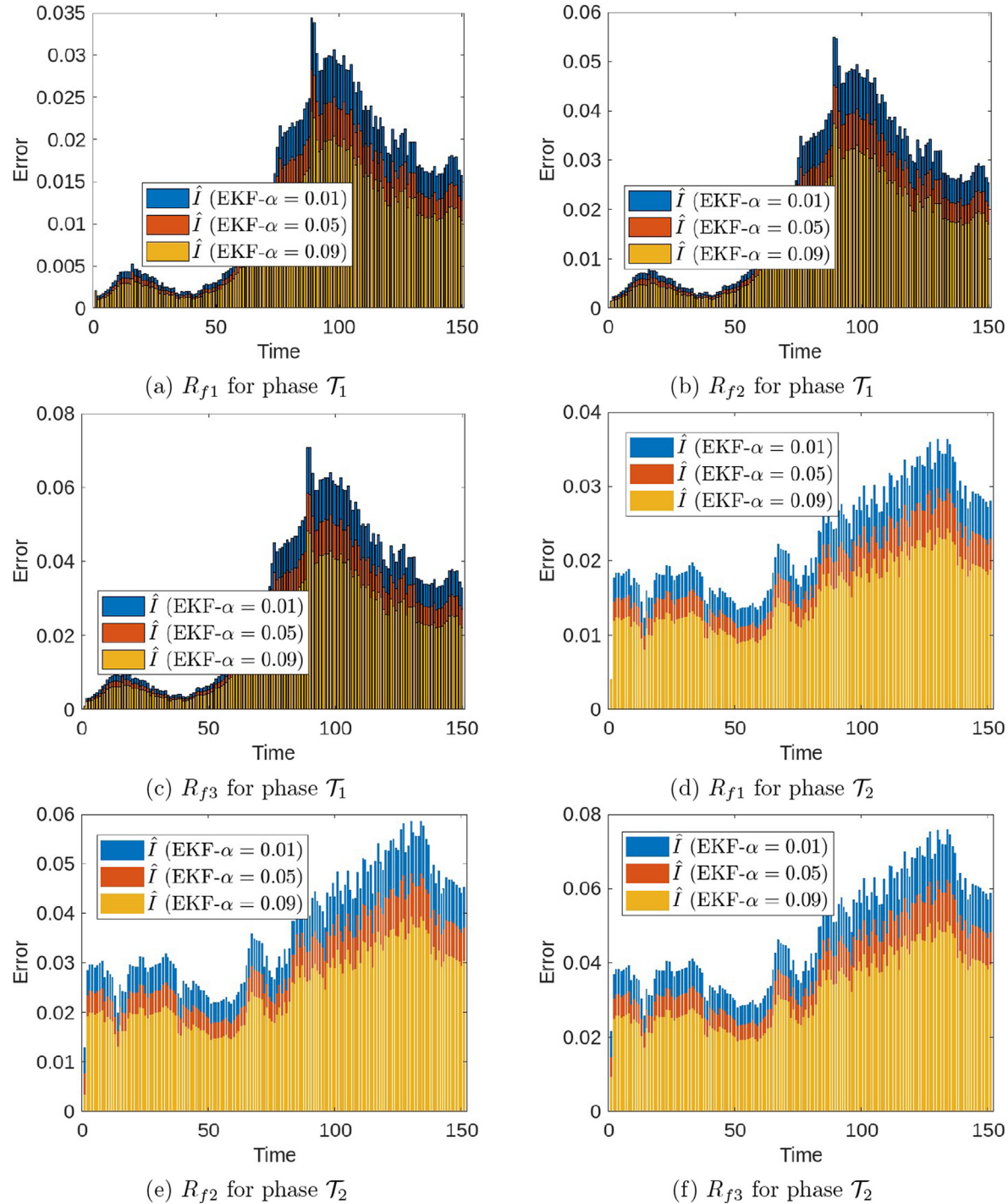


**Fig. 13.** Error values between predictions and reported data for various  $R_f : R_{f1} = (100; 10; 10; 1)$ ,  $R_{f2} = (200; 20; 20; 2)$ , and  $R_{f3} = (300; 30; 30; 3)$  in phases  $\mathcal{T}_1, \mathcal{T}_2$ .

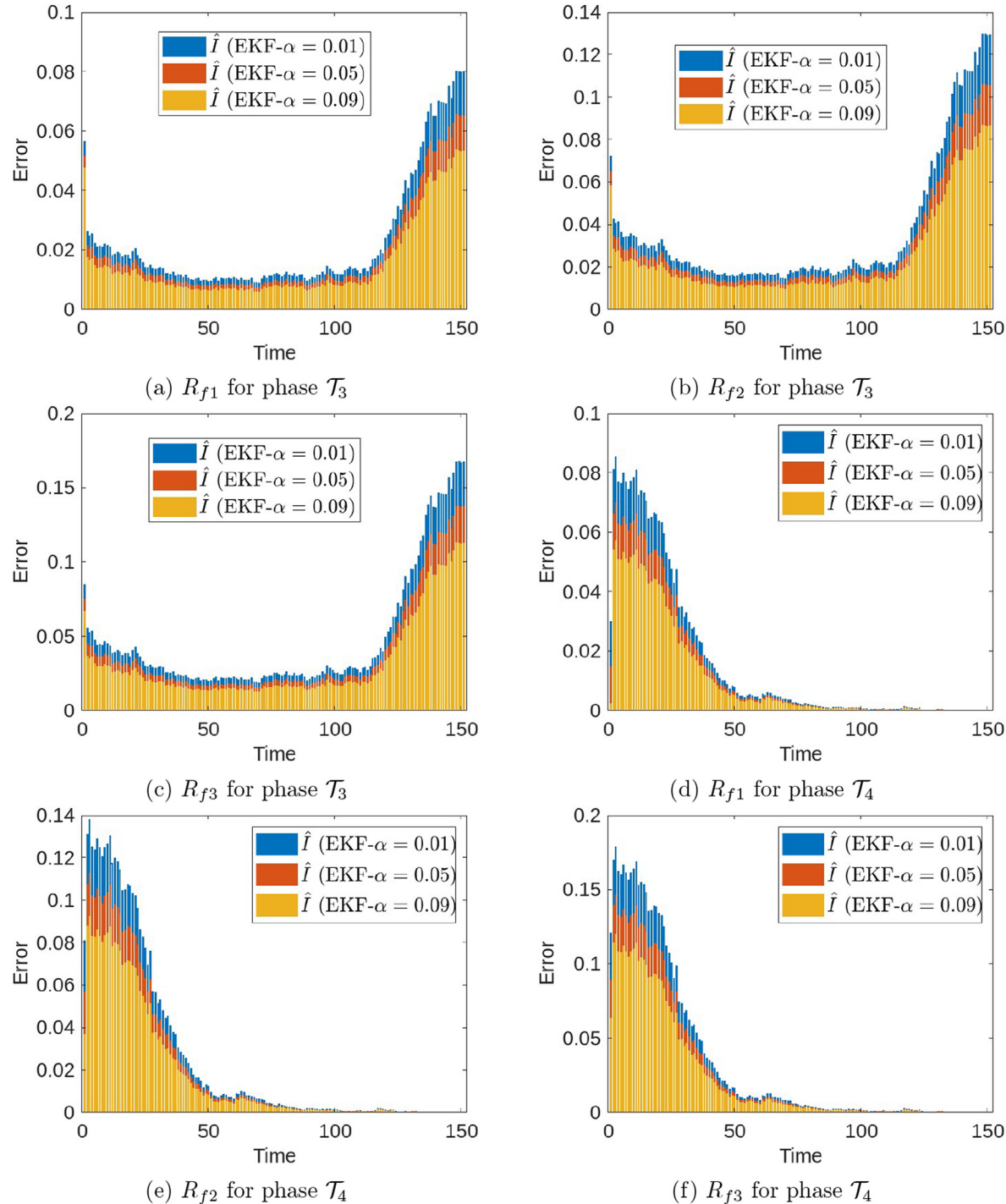


**Fig. 14.** Error values between predictions and reported data for various  $R_f : R_{f1} = (100; 10; 10; 1)$ ,  $R_{f2} = (200; 20; 20; 2)$ , and  $R_{f3} = (300; 30; 30; 3)$  in phases  $\mathcal{T}_3, \mathcal{T}_4$ .

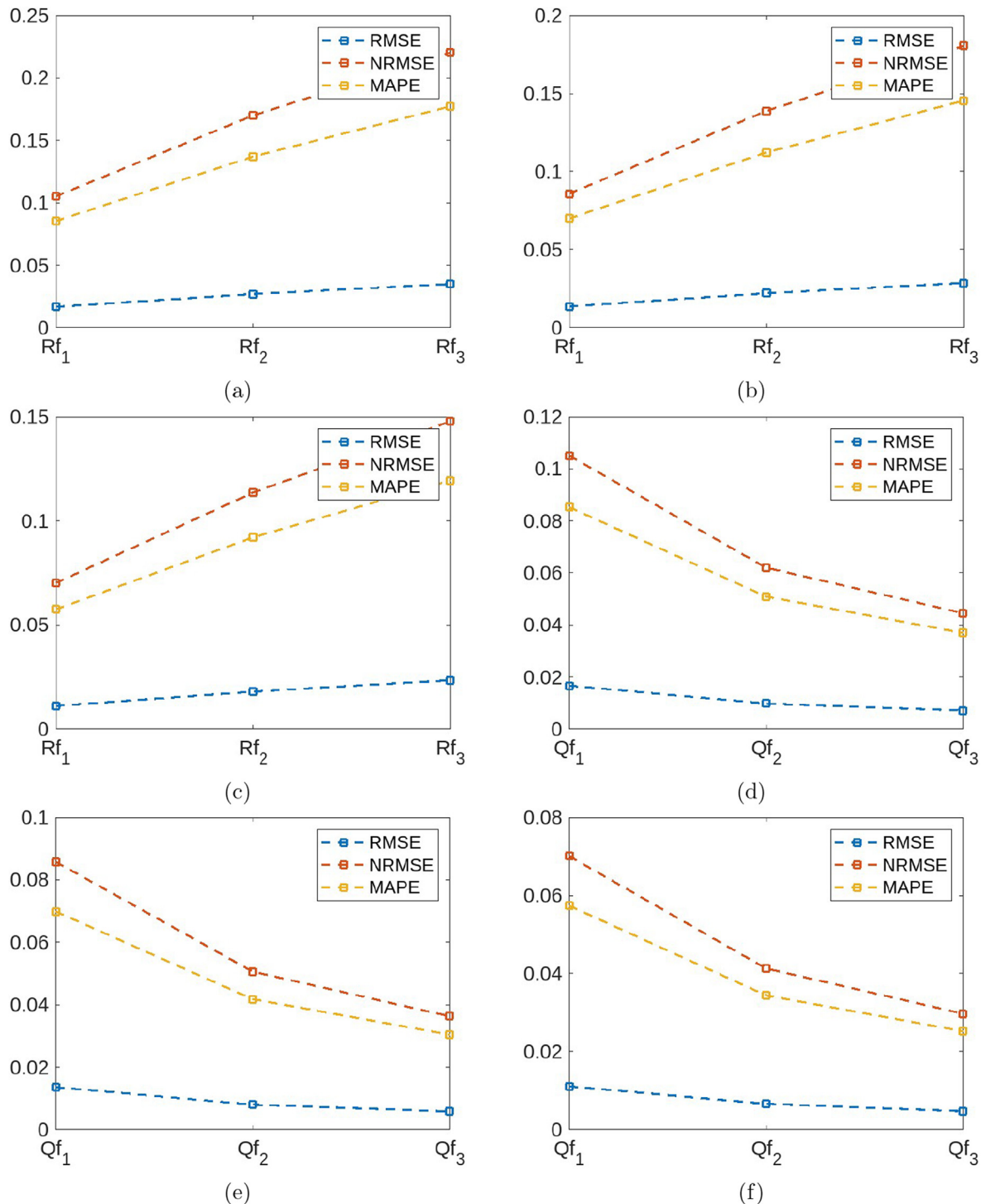


**Fig. 15.** Profiles of RMSE, NRMSE, and MAPE for various (a)–(c)  $R_f$  and (d)–(f)  $Q_f$ .

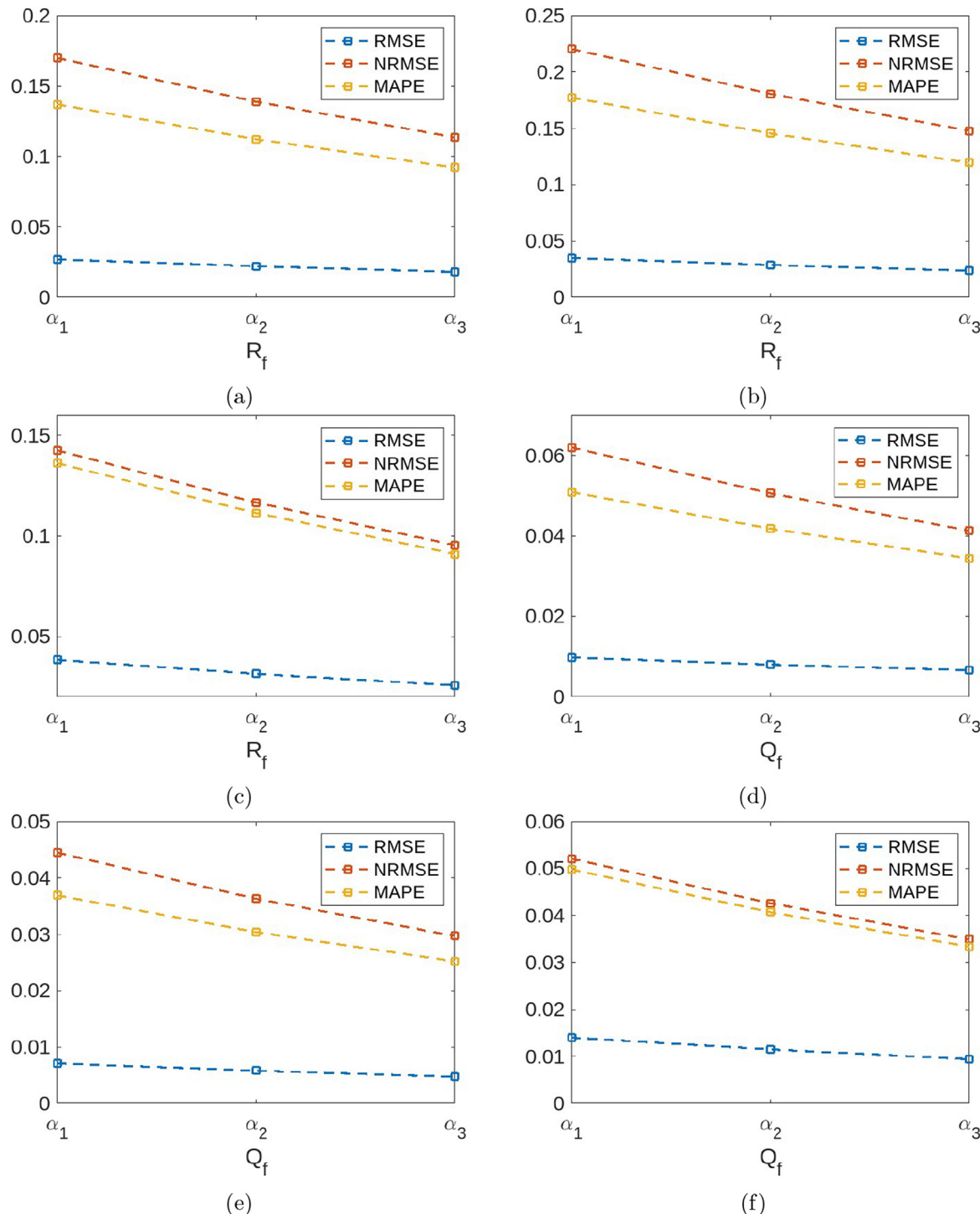


Fig. 16. Profiles of RMSE, NRMSE, and MAPE for various fractional-orders  $\alpha$  of (a)–(c)  $R_f$  and (d)–(f)  $Q_f$ .

## CRediT author statements

**Mohammad Ghani:** Conceptualization, Formal analysis, Investigation, Writing—original draft, Writing—review and editing, Software, **Dwi Rantini:** Formal analysis, Investigation, Methodology, Software, Writing—original draft, Writing—review and editing, **Maryamah:** Formal analysis, Investigation, Methodology, Software, Writing—original draft.

## Ethics statements

As an expert scientist, and along with my co-authors in the concerned field, this paper has been submitted with full responsibility, following due ethical procedure, and there is no duplicate publication, fraud, plagiarism, or concerns about animal or human experimentation.

## Declaration of Competing Interest

The authors declare that they have no known competing financial interests or personal relationships that could have appeared to influence the work reported in this paper.

## Acknowledgments

The authors would like to thank the reviewers for their valuable comments and suggestions, which helped to improve the paper. The first author received financial support for the research under contract number 121/UN3.1.17/PT/2022 from the Faculty of Advanced Technology and Multidiscipline, Universitas Airlangga, Indonesia.

## References

- Adnan et al. Investigation of time-fractional SIQR Covid-19 mathematical model with fractal-fractional Mittage-Leffler kernel. *Alexandria Eng J.* 2022;61 (10):7771–7779. <https://doi.org/10.1016/j.aej.2022.01.030>.
- Ahmed N, Raza A, Rafiq M, Ahmadian A, Batool N, Salahshour S. Numerical and bifurcation analysis of SIQR model. *Chaos Solitons Fractals.* 2021;150:111133. <https://doi.org/10.1016/j.chaos.2021.111133>.
- Alenezi MN, Al-Anzi FS, Alabdulrazzaq H. Building a sensible SIR estimation model for COVID-19 outspread in Kuwait. *Alexandria Eng J.* 2021;60 (3):3161–3175. <https://doi.org/10.1016/j.aej.2021.01.025>.
- Ali Z, Rabiei F, Rashidi MM, Khodadadi T. A fractional-order mathematical model for COVID-19 outbreak with the effect of symptomatic and asymptomatic transmissions. *Eur Phys J Plus* 2022;vol. 137, no. 3. doi: 10.1140/epjp/s13360-022-02603-z.
- Alqahtani RT. Mathematical model of SIR epidemic system (COVID-19) with fractional derivative: stability and numerical analysis. *Adv Differ Equ.* 2021;1:2021. <https://doi.org/10.1186/s13662-020-03192-w>.
- Alshammari FS, Khan MA. Dynamic behaviors of a modified SIR model with nonlinear incidence and recovery rates. *Alexandria Eng J.* 2021;60 (3):2997–3005. <https://doi.org/10.1016/j.aej.2021.01.023>.
- Annas S, Isbar Pratama M, Rifandi M, Sanusi W, Side S. Stability analysis and numerical simulation of SEIR model for pandemic COVID-19 spread in Indonesia. *Chaos Solitons Fractals.* 2020;139:110072. <https://doi.org/10.1016/j.chaos.2020.110072>.
- Ariffin MRK et al. Mathematical epidemiologic and simulation modelling of first wave COVID-19 in Malaysia. *Sci Rep.* 2021;11(1):1–10. <https://doi.org/10.1038/s41598-021-99541-0>.
- Arshad S, Khalid S, Javed S, Amin N, Nawaz F. Modeling the impact of the vaccine on the COVID-19 epidemic transmission via fractional derivative. *Eur Phys J Plus* 2022;vol. 137, no. 7. doi: 10.1140/epjp/s13360-022-02988-x.
- Atede AO, Omame A, Inyama SC. A fractional order vaccination model for COVID-19 incorporating environmental transmission: a case study using Nigerian data. *Bull Biomath.* 2023;1:78–110. <https://doi.org/10.59292/bulletinbiomath.2023005>.
- Baleanu D, Jajarmi A, Sajjadi SS, Mozyrska D. A new fractional model and optimal control of a tumor-immune surveillance with non-singular derivative operator. *Chaos.* 2019;29:083127. <https://doi.org/10.1063/1.5096159>.
- Baleanu D, Shekari P, Torkzadeh L, Ranjbar H, Jajarmi M, Nouri K. Stability analysis and system properties of Nipah virus transmission: a fractional calculus case study. *Chaos, Solitons and Fractals.* 2023;166:112990. <https://doi.org/10.1016/j.chaos.2022.112990>.
- Bani Younes A, Hasan Z. COVID-19: Modeling, prediction, and control. *Appl Sci* 2020;10 (11). doi: 10.3390/app1013666.
- Calafiore GC, Novara C, Possieri C. A time-varying SIRD model for the COVID-19 contagion in Italy. *Annu Rev Control.* 2020;50(October):361–372. <https://doi.org/10.1016/j.arcontrol.2020.10.005>.
- Cao Z, Feng W, Wen X, Zu L, Cheng M. Dynamics of a stochastic SIQR epidemic model with standard incidence. *Physica A.* 2019;527:1–12. <https://doi.org/10.1016/j.physa.2019.121180>.
- Cartocci A, Cevenini G, Barbini P. A compartment modeling approach to reconstruct and analyze gender and age-grouped CoViD-19 Italian data for decision-making strategies. *J Biomed Inform.* 2021;vol. 118, no. April:103793. <https://doi.org/10.1016/j.jbi.2021.103793>.
- Cooper I, Mondal A, Antonopoulos CG. A SIR model assumption for the spread of COVID-19 in different communities. *Chaos Solitons Fractals.* 2020;vol. 139, no. January:110057. <https://doi.org/10.1016/j.chaos.2020.110057>.
- Crokidakis N. CoVid-19 spreading in Rio de Janeiro, Brazil: Do the policies of physical isolation really work? *Chaos Solit Fract.* 2020;136:109930. <https://doi.org/10.1016/j.chaos.2020.109930>.
- Crokidakis N. Modeling the early evolution of the CoVid-19 in Brazil; results from Susceptible-Infectious-Quarantined-Recovered (SIQR). *Int J Mod Phys C.* 2020;31:1–8. <https://doi.org/10.1142/S0129183120501351>.
- Demongeot J, Griette Q, Magal P. SI epidemic model applied to COVID-19 data in mainland China. *R Soc Open Sci* 2020;vol. 7, no. 12. doi: 10.1098/rsos.201878.
- Diekmann O, Heesterbeek JAP, Metz JA. On the definition and the computation of the basic reproduction ratio  $R_0$  in models for infectious diseases in heterogeneous populations. *J Math Biol.* 1990(28):365–382. <https://doi.org/10.1007/BF00178324>.
- Defterli O, Baleanu D, Jajarmi A, Sajjadi SS, Alshaikh N, Asad JH. fractional treatment: an accelerated mass-spring system. *Roman Rep Phys.* 2022;74:122. <https://rrp.nipne.ro/2022/AN74122.pdf>.
- Diniz PSR, Filters Kalman. Adaptive filtering: algorithms and practical implementation. Cham: Springer International Publishing; 2020. 431–456. [https://doi.org/10.1007/978-3-030-29057-3\\_14](https://doi.org/10.1007/978-3-030-29057-3_14).
- Djalante R et al. Review and analysis of current responses to COVID-19 in Indonesia: Period of January to March 2020. *Prog Disast Sci.* 2020;6. <https://doi.org/10.1016/j.pdisas.2020.100091>.
- Fernandez PM, Fernandez-Muniz Z, Cernea A, Luis Fernandez-Martinez J, Kloczkowski A. Comparison of three mathematical models for COVID-19 prediction. *Biophys J* 2023;vol. 122, no. 3S1. doi: 10.1016/j.bpj.2022.11.1616.
- Fuady A, Nuraini N, Sukandar KK. Targeted vaccine allocation could increase the COVID-19 vaccine benefits amidst its lack of availability: a mathematical modeling study in Indonesia. *Vaccines (Basel).* 2021;9:462. <https://doi.org/10.3390/vaccines9050462>.
- Furati KM, Sarumi IO, Khaliq AQM. Fractional model for the spread of COVID-19 subject to government intervention and public perception. *Appl Math Model.* 2021;95:89–105. <https://doi.org/10.1016/j.apm.2021.02.006>.
- Ghani M, Utami IQ, Triayuda FW, Afifah M. A fractional SEIQR model on diphtheria disease. *Model Earth Syst Environ.* 2023;9:2199–2219. <https://doi.org/10.1007/s40808-022-01615-z>.
- Hasan A, Susanto H, Tjahjono VR, Kusdiantara R, Putri ERM, Hadisoemarto P, Nuraini N. A new estimation method for COVID-19 time-varying reproduction number using active cases. *Scient Rep.* 2022;12:6675. <https://doi.org/10.1038/s41598-022-10723-w>.
- Hamdan NI, Kilicman A. A fractional order SIR epidemic model for dengue transmission. *Chaos Solitons Fract.* 2018;114:55–62. <https://doi.org/10.1016/j.chaos.2018.06.031>.
- Hamdan NI, Kilicman A. Analysis of the fractional order dengue transmission model: a case study in Malaysia. *Adv Difer Equ.* 2019;114:3. <https://doi.org/10.1186/s13662-019-1981-z>.
- He S, Peng Y, Sun K. SEIR modeling of the COVID-19 and its dynamics. *Nonlinear Dyn.* 2020;101(3):1667–1680. <https://doi.org/10.1007/s11071-020-05743-y>.
- Khataee H, Scheuring I, Czirok A, Neufeld Z. Effects of physical distancing on the spreading of COVID-19 inferred from mobile phone data. *Sci Rep.* 2021;11 (1). doi: 10.1038/s41598-021-81308-2.
- Khoojine AS, Shadabfar M, Hosseini VR, Kordestani H. Network autoregressive model for the prediction of COVID-19 considering the disease interaction in neighboring countries. *Entropy.* 2021;23:1267. <https://doi.org/10.3390/e23101267>.
- Khoojine AS, Mahsuli M, Shadabfar M, Hosseini VR, Kordestani H. A proposed fractional dynamic system and Monte Carlo-based back analysis for simulating the spreading profile of COVID-19. *Eur Phys J Special Top.* 2022;231:3427–3437. <https://doi.org/10.1140/epjs/s11734-022-00538-1>.
- Kudryashov NA, Chmykhov MA, Vigdorowitsch M. Analytical features of the SIR model and their applications to COVID-19. *Appl Math Model.* 2021;90:466–473. <https://doi.org/10.1016/j.apm.2020.08.057>.
- Kumar S, Singh KK, Dixit P, Kumar Bajpai M. Kalman filter based short term prediction model for COVID-19 spread. *Appl Intell.* 2020;51(5):2714–2726. <https://doi.org/10.20546/ijcmas.2020.907.320>.
- Lin Y, Xu C, C. Finite difference/spectral approximations for the time-fractional diffusion equation. *J Comput Phys.* 2007;225(2):1533–1552. <https://doi.org/10.1016/j.jcp.2007.02.001>.
- Mahase E. Covid-19: What do we know about XBB.1.5 and should we be worried? *BMJ.* 2023;vol. 380, no. May:p153. <https://doi.org/10.1136/bmj.p153>.
- Marinov TT, Marinova RS. Adaptive SIR model with vaccination: simultaneous identification of rates and functions illustrated with COVID-19. *Sci Rep.* 2022;1–13. <https://doi.org/10.1038/s41598-022-20276-7>.
- Martinez V. A modified SIRD model to study the evolution of the covid-19 pandemic in Spain. *Symmetry (Basel)* 2021;vol. 13, no. 4. doi: 10.3390/sym13040723.
- Nanda MA et al. The susceptible-infected-recovered-dead model for long-term identification of key epidemiological parameters of COVID-19 in Indonesia. *Int J Electr Comput Eng.* 2022;12(3):2900–2910. <https://doi.org/10.11591/ijecce.v12i3.pp2900-2910>.
- Nwajeri UK, Panle AB, Omame A, Obi MC, Onyenegenecha CP. On the fractional order model for HPV and Syphilis using non-singular kernel. *Results Phys.* 2022;37:105463. <https://doi.org/10.1016/j.rinp.2022.105463>.
- Nwajeri UK, Omame A, Onyenegenecha CP. Analysis of a fractional order model for HPV and CT co-infection. *Results Phys.* 2021;28:104643. <https://doi.org/10.1016/j.rinp.2021.104643>.
- Odagaki T. Analysis of the outbreak of COVID-19 in Japan by SIQR model. *Infect Dis Model* 1982;vol. 5, no. May: p. 691–8. doi: 10.1016/j.idm.2020.08.013.
- Omame A, Onyenegenecha IP, Raeza AA, Rihan FA. Co-Dynamics of COVID-19 and Viral Hepatitis B using a mathematical model of non-integer order: impact of vaccination. *Fractal Fract.* 2023;7:544. <https://doi.org/10.3390/fractfract7070544>.

47. Omame A, Zaman FD. Analytic solution of a fractional order mathematical model for tumour with polyclonality and cell mutation. *Partial Differ Eq Appl Math.* 2023;8:100545. <https://doi.org/10.1016/j.padiff.2023.100545>.
48. Panigoro HS, Suryanto A, Kusumawinahyu WM, Darti I. Dynamics of a fractional-order predator-prey model with infectious diseases in prey. *Commun Biomath Sci.* 2019;2:105–117. <https://doi.org/10.5614/cbms.2019.2.2.4>.
49. Parhusip HA, Trihandaru S, Wicaksono BAA, Indrajaya D, Sardjono Y, Vyas OP. Susceptible Vaccine Infected Removed (SVIR) Model for COVID-19 Cases in Indonesia. *Sci Technol Indonesia.* 2022;7(3):400–408. <https://doi.org/10.26554/sti.2022.7.3.400-408>.
50. Podlubny I. *Fractional differential equations: an introduction to fractional derivatives, fractional differential equations, to methods of their solution and some of their applications.* California CA, USA: Academic Press; 1999.
51. Sadek L, Sadek O, Alaoui HT, Abdo MS, Shah K, Abdeljawad T. Fractional order modeling of predicting COVID-19 with isolation and vaccination strategies in Morocco. *Comput Model Eng Sci.* 2023;136:1931–1950. <https://doi.org/10.32604/cmes.2023.025033>.
52. Sameni R. Mathematical Modeling of epidemic diseases; a case study of the COVID-19 Coronavirus, 2020 arXiv preprint arXiv:2003.11371, <https://doi.org/10.48550/arXiv.2003.11371>.
53. Sepulveda G, Arenas AJ, González-Parra G. Mathematical modeling of COVID-19 dynamics under two vaccination doses and delay effects. *Mathematics.* 2023;11(2):1–30. <https://doi.org/10.3390/math11020369>.
54. Shadabfar M, Mahsuli M, Khojine AS, Hosseini VR. Time-variant reliability-based prediction of COVID-19 spread using extended SEIVR model and Monte Carlo sampling. *Results Phys.* 2021;26:104364. <https://doi.org/10.1016/j.rinp.2021.104364>.
55. Shadabfar M, Mahsuli M, Khojine AS, Hosseini VR, Hong A. Randomized fractional SEIR-VQHP model with applications in covid-19 data prediction. *Fractals.* 2023;31:2340064. <https://doi.org/10.1142/S0218348X23400649>.
56. Shah K, Sinan M, Abdeljawad T, El-Shorbagy MA, Abdalla B, Abualrub MS. A detailed study of a fractal-fractional transmission dynamical model of viral infectious disease with vaccination. *Complexity.* 2022;1–21:2022. <https://doi.org/10.1155/2022/7236824>.
57. Sinan M, Ansari KJ, Kanwal A, Shah K, Abdeljawad T, Zakirullah, Abdalla B. Analysis of the mathematical model of cutaneous Leishmaniasis disease. *Alexandria Eng J.* 2023;72:117–134. <https://doi.org/10.1016/j.aej.2023.03.065>.
58. Song J, Xie H, Gao B, Zhong Y, Gu C, Choi KS. Maximum likelihood-based extended Kalman filter for COVID-19 prediction. *Chaos Solit Fract.* 2021;146:110922. <https://doi.org/10.1016/j.chaos.2021.110922>.
59. Suryanto A, Darti I, Panigoro HS, Kilicman A. A fractional-order predator-prey model with ratio-dependent functional response and linear harvesting. *Mathematics.* 2019;7:1100. <https://doi.org/10.3390/math7111100>.
60. ud Din R, Algehyne EA. Mathematical analysis of COVID-19 by using SIR model with convex incidence rate. *Results Phys.* 2020;vol. 23, no. October: p. 1–6. doi: 10.1016/j.rinp.2021.103970.
61. Yangla J et al. Fractional dynamics of a Chikungunya transmission model. *Sci Afr.* Sep. 2023;21. <https://doi.org/10.1016/j.sciaf.2023.e01812>.
62. Zhang R, Liu Y. A new Barbalat's lemma and Lyapunov stability theorem for fractional order systems. *29th Chinese control and decision conference (CCDC).* IEEE; 2017. 3676–3681. <https://doi.org/10.1109/CCDC.2017.7979143>.
63. Zhu X, Gao B, Zhong Y, Gu C, Choi KS. Extended Kalman filter for online soft tissue characterization based on Hunt-Crossley contact model. *J Mech Behav Biomed Mater.* 2021;123:104667. <https://doi.org/10.1016/j.jmbbm.2021.104667>.